Near East Desertification: impact of Dead Sea drying on the local conditions leading to convection

Samiro Khodayar[1,2] and Johannes Hoerner[2]

[1]Institute of Meteorology and Climate Research (IMK-TRO), Karlsruhe Institute of Technology (KIT), Karlsruhe, Germany

[2]Mediterranean Centre for Environmental Studies (CEAM), Valencia, Spain

Submitted to Atmospheric Chemistry and Physics

(HyMeX Inter-journal SI)

* Corresponding author. E-mail address: Khodayar_sam@gva.es (S. Khodayar)

Mediterranean Centre for Environmental Studies (CEAM),

Technological Park, Charles R. Darwin Street, 14 46980 - Paterna - Valencia - Spain

Abstract

The Dead Sea desertification-threatened region is affected by continual lake level decline and occasional, but life-endangering flash-floods. Climate change has aggravated such issues in the past decades. In this study, the impact of the Dead Sea drying on the severe convection generating heavy precipitation in the region is investigated. Sensitivity simulations with the high-resolution convection-permitting regional climate model COSMO-CLM and several numerical weather prediction (NWP) runs on an event time scale are performed over the Dead Sea area. A reference simulation covering the 2003 to 2013 period and a twin sensitivity experiment, in which the Dead Sea is dried out and set to bare soil, are compared. NWP simulations focus on heavy precipitation events exhibiting relevant differences between the reference and the sensitivity decadal realization to assess the impact on the underlying convection-related processes.

The drying of the Dead Sea is seen to affect the atmospheric conditions leading to convection in two ways: (a) the local decrease in evaporation reduces moisture availability in the lower boundary layer locally and in the neighbouring, directly affecting atmospheric stability. Weaker updrafts characterize the drier and more stable atmosphere of the simulations where the Dead Sea has been dried out. (b) Thermally driven wind system circulations and resulting divergence/convergence fields are altered preventing in many occasions convection initiation because of the omission of convergence lines. On a decadal scale, the difference between the simulations suggests that in future regional climate, under ongoing lake level decline, a decrease in evaporation, higher air temperatures and less precipitation may be expected.

Key Words: Dead Sea drying, climate change, convection, heavy precipitation, boundary layer, wind systems, *high-resolution modelling*

1. Introduction

The Eastern Mediterranean and the Middle East is a sensitive climate change area (Smiatek et al. 2011). The anticipated warming in the 21st century combined with the general drying tendency, suggest important regional impacts of climate change, which should be investigated to assess and mitigate local effects on society and ecosystems. The Dead Sea basin is dominated by semi-arid and arid climates except by the north-western part that is governed by Mediterranean climate (Greenbaum et al. 2006). It is an ideal area to study climate variation in the Near East. It was already discussed by Ashbel (1939) the influence of the Dead Sea on the climate of its neighbouring regions. The change in the climate of the Dead Sea basin caused by the drying of the Dead Sea has also been evidenced in the last decades (Alpert et al. 1997; Cohen and Stanhill 1996; Stanhill 1994). The Dead Sea is the lowest body of water in the world (~ -430 m) surrounded by the Judean Mountains (up to ~ 1 km amsl) to the west and to the east by the Maob Mountains (up to ~ 3 km amsl). The area in between is rocky desert. The complex topography of the area favours the combined occurrence of several wind regimes in addition to the general synoptic systems, namely valley and slope winds, Mediterranean breezes and local lake breezes (e.g. Shafir and Alpert 2011). These wind systems are of great importance for the living conditions in the region since they influence the visibility and the air quality (e.g. Kalthoff et al. 2000; Corsmeier et al. 2005) as well as the atmospheric temperature and humidity. Since the Dead Sea is a terminal lake of the Dead Sea Valley, no natural outflow exists, being evaporation the main loss of water, being the wind velocity and vapour pressure deficit identified as the main governing factors of evaporation throughout the year (Metzger et al. 2017). Through the high evaporation the lake level declines and results in a desertification of the shoreline and a changing fraction of water and land surface in the valley. The documented Dead Sea water level drop of about 1 m/y in the last decades (Gavrieli et al. 2005) is mainly due to the massive water consumption at its upstream having climate changes a small contribution to the lake level decrease (Lensky and Dente 2015). This situationseverely affects agriculture, industry and the environmental conditions in the area, thus, leading to substantial economic losses (Arkin and Gilat 2000).

The Jordan River catchment and Dead Sea exhibit in the north, annual precipitation in the order of 600-800 mm, whereas in the south, there is an all year arid climate with an annual precipitation of <150 mm (Schaedler and Sasse 2006). Rain occurs between October and May and can be localized or widespread (Dayan and Sharon 1980) (Sharon and Kutiel 1986). Rainfall varies seasonally and annually, and it is often

concentrated in intense showers (Greenbaum et al. 2006) caused mainly by severe convection (Dayan and Morin 2006). Flash floods are among the most dangerous meteorological hazards affecting the Mediterranean countries (Llasat et al 2010), thus, knowledge about the processes shaping these events is of high value. This is particularly relevant in arid climates, where rainfall is scarce, and often, local and highly variable. In flood-producing rainstorms, atmospheric processes often act in concert at several scales. Synoptic-scale processes transport and redistribute the excess sensible and latent heat accumulated over the region and subsynoptic scale processes determine initiation of severe convection and the resulting spatio-temporal rainfall characteristics. The main responsible synoptic weather patterns leading to heavy rainfall in the region are in general well known and described in previous publications (e.g. Belachsen et al. 2017; Dayan and Morin 2006). Belachsen et al. (2017) pointed out that three main synoptic patterns are associated to these heavy rain events: Cyprus low accounting for 30% of the events, Low to the east of the study region for 44%, and Active Read Sea Trough for 26%. The first two originate from the Mediterranean Sea, while the third is an extension of the Africa monsoon. Houze (2012) showed that orographic effects lead to enhanced rainfall generation; rain cells are larger where topography is higher. Sub-synoptic scale processes play a decisive role in deep convection generation in the region. Convection generated by static instability seems to play a more important role than synoptic-scale vertical motions (Dayan and Morin 2006). The moisture for developing intensive convection over the Dead Sea region can be originated from the adjacent Mediterranean Sea (Alpert und Shay-EL 1994) and from distant upwind sources (Dayan and Morin 2006).

In this study, the drying of the Dead Sea is investigated focusing on the impact on atmospheric conditions leading to heavy precipitating convection in the region. The relevance of the Dead Sea as a local source of moisture for precipitating convection as well as the impact of the energy balance partitioning changes and related processes caused by the drying of the Dead Sea are investigated. With this purpose, a sensitivity experiment with the high-resolution regional climate model COSMO-CLM [Consortium for Small scale Modelling model (COSMO)-in Climate Mode (CLM); Böhm et al. 2006] is conducted. The high horizontal grid spacing used (~ 2.8 km) resolves relevant orographic and small-scale features of the Dead Sea basin, which is not the case when coarser resolution simulations are performed. Moreover, at this resolution convection is explicitly resolved instead of being parametrized, which has been already extensively demonstrated to be highly beneficial for the simulation of heavy precipitation and convection-related processes. The benefit of employing high-resolution convection

permitting simulations is mainly in sub-daily time-scales, (e.g., Prein et al., 2013; Fosser et al., 2014; Ban et al., 2014), however, daily precipitation is also positively affected, particularly in winter time (Fosser et al., 2014). Previous studies in the area applying high-resolution modelling agree with the benefitial impact of finer resolution against coarser ones (e.g. *Rostkier-Edelstein et al. 2014; Hochman et al. 2018; Kunin et al. 2019*).

The impact of completely drying the Dead Sea on the regional atmospheric conditions and precipitating convection is discussed. A decadal simulation and several event-based Numerical Weather Prediction (NWP) runs covering the eastern Mediterranean are carried out. A process understanding methodology is applied to improve our knowledge about how sub-synoptic scale processes leading to severe convection are affected by the drying of the Dead Sea. The article is organized as follows. Section 2 provides an overview of the data and the methodology used. Then, in section 3, the climatology of the region based on the high-resolution convection-permitting decadal simulation is presented and the impact of drying the Dead Sea is examined across scales. Finally, conclusions are discussed in section 4.

2. Data and methodology

2.1 The COSMO-CLM model

In this investigation, the regional climate model (RCM) of the non-hydrostatic COSMO model, COSMO-CLM (CCLM), is used (Version 5.0.1). It has been developed by the Consortium for Small-scale modeling (COSMO) and the Climate Limited-area Modeling Community (CLM) (Böhm et al., 2006). It uses a rotated geographical grid and a terrain-following vertical coordinate. The model domain covers the southern half of the Levant, centred around the Dead Sea, with a horizontal resolution of 7 km and 2.8 km, 60 vertical levels and a time step of 60 and 20 seconds, respectively. Using IFS (Integrated Forecasting System) analysis, the spectral weather model of ECMWF (European Centre for Medium-Range Weather Forecast) as driving data for the simulations, a double nesting procedure was employed. The coarsest nest at 0.0625º resolution (about 7 km) covers 250 grid points in x direction and 250 grid points in y direction. The size and location of the 7 km domain has been considered large enough to have into consideration all possible synoptic situations relevant for the development of extreme phenomena in the study area as well as the influence of the Mediterranean Sea. The finest nest at 0.025º (circa 2.8 km) covers 150 x 150 grid points, thus a total

area of 22500 grid points and includes the study area (72 grid point in x direction and 92 in y direction) centred around the Dead Sea.

A Tiedtke (1989) mass-flux scheme is used for moist convection in the 7 km, and reduced Tiedke mass-flux scheme for shallow convection. Contrary to the CCLM-7 km simulation, where convection is parameterized, in the CCLM-2.8 km convection is explicitly resolved (Doms and Baldauf, 2015), so only the reduced Tiedke mass-flux scheme is used for shallow convection. The model physics includes a cloud physics parameterization with 5 types of hydrometeors (water vapor, cloud water, precipitation water, cloud ice, precipitation ice), a radiative transfer scheme based on a delta-two-stream solution (Ritter and Geleyn, 1992) and a roughness-length dependent surface flux formulation based on modified Businger relations (Businger et al., 1971).

Orography data from GLOBE (Global Land One-km Base Elevation Project) of NOAA (National Oceanic and Atmospheric Administration) and soil data from HWSD (Harmonized Worlds Soil Database) TERRA is used. HWSD is a global harmonization of multiple regional soil data sets with a spatial resolution of 0.008° (FAO, 2009), resulting in 9 different soil types in the model, namely ‘ice and glacier', 'rock / lithosols', 'sand', 'sandy loam', 'loam', 'loamy clay', 'clay', 'histosols', and 'water'.

Multiple model runs have been performed. A 7 km run from 2003 to 2013 with dailyoutput is used as nesting for two 2.8 km runs over the same time span. The Dead Sea is dried out and replaced with soil types from the surrounding area in one of them (SEN), the other one is used as reference (CLIM). For the detailed investigation of convective events on 14.11.2011 and 19.11.2011, sub-seasonal simulations have been performed with the same settings as the decadal simulation, but with hourly outputs due to the limitations imposed by the daily output.

2.2 Methodology

In order to assess the impact of the drying of the Dead Sea on the atmospheric conditions leading to severe convection in the region, a set of sensitivity experiments was performed. A decadal simulation covering the 2003 to 2013 time period was carried out with the convection permitting 2.8 km COSMO-CLM model. Lateral boundary conditions and initial conditions are derived from the European Centre for Medium-Range Weather Forecasts (ECMWF) data. The COSMO-CLM 7 km is used as nesting step in between the forcing data and the 2.8 km run. This reference simulation will be hereafter referred to as REF^{CLIM} simulation. Parallel to this, a sensitivity experiment (hereafter SEN^{CLIM}) is carried out in which the Dead Sea is dried out and

172 set to bare soil on -405 m level (depth of the Dead Sea in the external data set, GLOBE
173 (Hastings and Dunbar, 1999)). After examination of the results, the first year of
174 simulations is considered spin-up time, thus, our analysis covers the 2004-2013 period.

175 The precipitation field has been validated using the EOBS dataset (Haylock et al. 2008)
176 with a resolution of 0.1° and available for the period 1980-2011, and the APHRODITE's
177 (Asian Precipitation - Highly-Resolved Observational Data Integration Towards
178 Evaluation: Yatagai et al. 2008, 2012) daily gridded precipitation which is the only long-
179 term continental-scale daily product that contains a dense network of daily rain-gauge
180 data for Asia. It has a resolution of 0.25º and is available for 1980-2007. The
181 APHRODITE data shows generalized lower precipitation values than EOBS, but still
182 higher than our simulation particularly close to the northern Mediterranean shoreline,
183 over coastal-flat terrain, whereas the best agreement is at areas dominated by complex
184 terrain. This agrees with previous high-resolution modelling activities in the region such
185 as Rostkier-Edelstein et al. (2014) using WRF at 2 km. They suggest in this publication
186 that inaccuracies in the gridded SST dataset used in the simulations could be
187 responsible for the observed bias highlighting the strong sensitivity of precipitation in
188 the Mediterranean basin to very small differences in the SST (Miglietta et al. 2011).
189 Despite these biases the comparison of the temporal areal-mean of the model
190 simulations at 7 km and 2.8 km and the APHRODITE dataset demonstrates that in
191 general the model quiete well captures the precipitation events. An improvement is
192 seen at the finer resolution.

193 Regional dry and wet periods are identified and quantified in the simulations by means
194 of the Effective Drought Index (EDI; Byun and Wilhite 1999; Byun and Kim 2010). The
195 EDI is an intensive measure that considers daily water accumulations with a weighting
196 function for time passage normalizing accumulated precipitation. The values are
197 accumulated at different time scales and converted to standard deviations with respect
198 to the average values. Here we use an accumulation period of 365 days. EDI dry and
199 wet periods are categorized as follows: moderate dry periods -1.5 <EDI<-1, severe dry
200 periods -2<EDI<-1.5, and extreme dry periods EDI<-2. Normal periods are revealed by
201 -1<EDI<1 values.

202 Based on daily mean values, precipitation and evapotranspiration distribution and
203 possible tendencies in the 10-year period are assessed. To further asses the most
204 affected areas in our study area, this is divided in four subdomains surrounding the
205 Dead Sea and trying to respect the orographic pattern in the area (Figure 3). Annual
206 cycles are thus separately investigated to take into consideration the relevant

differences in orography, soil types, and distance to the coast among others (Figure1), which are known to have a significant impact in the precipitation distribution in the region (e.g. Belachsen 2017; Houze 2012). . Differences in the annual cycle and temporal evolution of precipitation and evapotranspiration between the REF^{CLIM} and SEN^{CLIM} are discussed. Also, differences in the near-surface and boundary layer conditions and geopotential height patterns are examined. Geographical patterns of mean evapotranspiration and precipitation and differences with respect to the reference simulation are assessed. Probability distribution functions (PDFs), and the Structure, Amplitude and Location (SAL: Wernli et al. 2008) analysis methodologies are used to illustrate differences in the mean and extreme precipitation between the reference and the sensitivity experiments. The SAL is an object-based rainfall verification method. This index provides a quality measure for the verification of quantitative precipitation forecasts considering three relevant aspects of precipitation pattern: the structure (S), the amplitude (A), and the location (L). The A component measures the relative deviation of the domain-averaged rainfall; positive values indicate an overestimation of total precipitation, negative values an underestimation. The component L measures the distance of the center of mass of precipitation from the modelled one, and the average distance of each object from the center of mass. The component S is constructed in such a way that positive values occur if precipitation objects are too large and/or too flat and negative values if the objects are too small and/or too peaked, quantifying the physical distance between the centres of mass of the two rainfall fields to be compared. Perfect agreement between prediction and reference are characterized by zero values for all components of SAL. Values for the amplitude and structure are in the range (−2, 2), where ±0.66 represents a factor of 2 error. The location component ranges from 0 to 2, where larger values indicate a greater separation between centres of mass of the two rainfall fields. This is done by selecting a threshold value of 1/15 of the maximum rainfall accumulation in the domain (following Wernli et al. 2008). The structure and location components are thus independent of the total rainfall in the domain.

Differences in the temporal evolution of precipitation between the REF^{CLIM} and SEN^{CLIM} are identified. In Table 1, those events in which an area-mean (study area, Figure 1) difference between both simulations higher than ±0.1 mm/d exists are selected as potential heavy precipitation events and classified attending to their synoptic scale environment, and atmospheric stability conditions (Table 1).

Although Dayan and Morin (2006) discuss that in general large-scale vertical motions do not provide the sufficient lifting necessary to initiate convection, it was demonstrated

by Dayan and Sharon (1980) that a relationship exists between the synoptic-scale weather systems and deep moist convection, being those systems responsible for the moisturizing and destabilization of the atmosphere prior to convective initiation. They pointed out that indices of instability proved the most efficient determinants of the environment characterizing each rainfall type in the region. Thus, two indicators of the atmospheric degree of stability/instability, namely the Convective Available Potential Energy (CAPE; Moncrieff and Miller 1976) and the KO-index (Andersson et al. 1989), are examined in this study. The CAPE is a widely known index indicating the degree of conditional instability. Whereas, the KO-index, which is estimated based on the equivalent potential temperature at 500, 700, 850 and 1000 hPa (following the recommendations by Bolton 1980), describes the potential of deep convection to occur as a consequence of large-scale forcing (Andersson et al. 1989; Khodayar et al. 2013). Generally, regions with KO-index < 2 K and large-scale lifting are identified as favourable for deep convection. Parcel theory (50 hPa ML (Mixed Layer) parcel) and virtual temperature correction (Doswell and Rasmussen 1994) are applied to these calculations.

Based on the above criteria, a separation was made between events with widespread rainfall and those more localized. Among the latter, we selected two events to illustrate the local impacts on the boundary layer conducive to deep moist convection. Particularly, differences in the amount, structure and location of precipitation are assessed by examining the spatial patterns and the SAL verification method. The two selected events for detail analysis in this study are those showing the larger SAL deviations. Those two cases occur close in time. Carefull inspection of the atmospheric conditions after the first event shows no significant differences between simulations suggesting no connetion between both events.Even though a more detail analysis is provided for the two selected cases, all convective-events listed in Table 1 have been examined to assess the main impacts on the mechanisms leading to convection. High-resolution simulations with the NWP COSMO 2.8 km model are performed with hourly output temporal resolution and covering a 3-day period (including 48-h prior to the day of the event, from 00 UTC) to capture atmospheric pre-conditions conducive to deep moist convection. For this, a reference simulation, REF^{NWP}, and a sensitivity experiment, SEN^{NWP}, are carried out for each event.

3. Results and discussion

3.1 Climatology of the Dead Sea region

Annual cycle

To assess the climatology of the study region (Figure 1) the annual evaporation and precipitation cycles based on daily means of the respective quantities are investigated (Figure 2). Additionally, we examine the evolution of specific humidity (Qv_{2m}) and temperature at 2 m (T_{2m}) as well as total column integrated water vapour (IWV) and low-boundary layer (< 900 hPa) equivalent potential temperature (Θ_e). Possible changes in the atmospheric stability conditions are evaluated by examination of the CAPE and KO-index. In Figure 2, all grid points over the study region (Figure 1) and the time period 2004-2013 are considered. Differences between the REF^{CLIM} and the SEN^{CLIM} simulations are also discussed.

The annual cycle of evaporation shows minimum values in the autumn season (around October, ~ 0.1 mm/d) and maximum evaporation in spring (around March, ~ 0.4 mm/d). The dependency with the precipitation cycle is clear with maximum values of the latter around March and rain occurring between October and May (Figure 2a) in agreement with observations in the area (Dayan and Sharon 1980). The difference between the evaporation in the REF^{CLIM} and the SEN^{CLIM} simulations indicates a mean decrease in the order of 0.02 (February) to ~ 0.1 (August) mm/d in the absence of the Dead Sea water (SEN^{CLIM}). The largest difference is in the dry period (May to October) when water availability is less dependent on precipitation, and evaporation is higher over the Dead Sea in contrast to the minimum values over land (Metzger et al. 2017). In general, there is a decrease of about 0.5 % in precipitation in the SEN^{CLIM} simulation. In contrast to the differences in evaporation, precipitation differences between the reference and the sensitivity experiment occur in both directions during the rain period, from October to May. Examining the total number over the whole decadal simulation it is seen that the number of dry or wet days (> 0.1 mm/d) or heavy precipitation events is not largely affected in the sensitivity experiment. In general, the number of dry days increases (fewer wet days) in the SEN^{CLIM} simulation, whereas the number of high intensity events show almost no variation. For each simulation, the difference between precipitation and evaporation is negative mainly in spring and summer contributing to the dryness in the region. Furthermore, the negative difference between the REF^{CLIM} and SEN^{CLIM} simulations indicates that the PREC-EVAP difference is higher in the SEN^{CLIM} simulation probably in relation to the reduced evaporation over the dry sea area and the general decrease in the precipitation amount in the region.

In addition to the reduced evaporation and precipitation (about 0.5 %) in the whole domain in the SEN^{CLIM} simulation a drier and warmer lower-troposphere is identified

(Figure 2b) in agreement with the observational assessment by Metzger et al. (2017) of the cooling effect of evaporation on air temperature in the region. The annual cycle of IWV and $\Theta_{e<900hPa}$ in Figure 2c show that the impact of the dry Dead Sea resulting evaporation is less pronounced when a deeper atmospheric layer is considered. Indeed, $\Theta_{e<900hPa}$ evolution evidences that the warming effect due to the decreased evaporation in the SEN^{CLIM} simulation is restricted to the near surface.

In Figure 2d, the annual cycle of areal mean CAPE displays larger values in the period from August to November, being this the period more favourable for convection. Positive CAPE differences between the REF^{CLIM} and the SEN^{CLIM} simulations are presumably in relation to the identified distinct lower-atmospheric conditions, being these more favourable and consequently CAPE values higher in the REF^{CLIM} simulation. In the same period, the KO-index indicates a more potentially unstable atmosphere, i.e. prone to deep convection because of large-scale forcing, and larger differences between simulations.

In agreement with the well-known precipitation distribution in the region most of the events occur in A1 (north-west) and A2 (north-east). Also, in these subdomains larger differences between the REF^{CLIM} and SEN^{CLIM} simulations are identified pointing out the relevance of the Dead Sea evaporation in the pre-convective environment for rainfall episodes over the study area (Figure3a). Considering only land grid points almost no difference between simulations is found in the evaporation annual cycle of A1 and A2 (Figure3b) suggesting the distinct amount of moisture advected towards A1 and A2 from the Dead Sea in REF^{CLIM} and SEN^{CLIM} as responsible for the differences in the boundary layer conditions conducive to convection. Also, in these subdomains the dryer and warmer lower boundary layer and the reduced instability in the SEN^{CLIM} are recognized

Inter-annual variability

In Figures 4 we discuss the inter-annual variability (based on monthly-daily areal mean values) of evaporation, precipitation as well as drought evolution.

The reduced evaporation in the annual cycle of the SEN^{CLIM} simulation for the whole investigation domain, resulting from the drying of the Dead Sea and affected evaporation, remains from year to year (Figure 4a). Larger differences between the simulations occur in the May to November months in agreement with the annual cycle in Figure 2a. This, and the time period of the maximum/minimum is constant over the years. A tendency towards lower evaporation at each simulation and higher differences

between both at the end of the period are identified. An inter-annual fluctuation is observed in both REF^{CLIM} and SEN^{CLIM} simulations. The yearly rate of evaporation shows, for example, in REF^{CLIM} maximum values of about 7 mm in 2011 and around 17 mm in 2012. This is in agreement with the positive correlation expected between precipitation and evaporation, a trend towards decreased precipitation and a correspondence between drier years such as the 2011-2012 period and lower annual evaporation are seen in Figure 4b. Year to year EDI calculations in Figure 4c help us identify the regional extreme dry and wet periods. The EDI range of variation from about -1 to 2 for the whole period of simulation indicates that the dry condition is the common environment in the area, while the wet periods, EDI up to 6, could be identified as extreme wet periods (relative to the area), in this case in the form of heavy precipitation events. Maximum positive EDI values are in the first months of the year in agreement with the precipitation annual cycle in Figure 2, whereas minimal EDI values occur in summer and autumn indicative of the dry conditions in these periods. Differences in the EDI calculations from both simulations reveal distinct precipitation evolutions and denote timing differences in the occurrence of the precipitation events. When the regional climate evolution is examined in combination with the impact on the number of heavy precipitation events (Table 1) the impact is stronger in the dry period of 2011 (Figure 4a). About six events show relevant differences in this period, contrary to the average 3 episodes per year.

Spatial distribution

The geographical patterns of evaporation and precipitation are presented in Figure 5. Over the Dead Sea, the simulated average annual evaporation for the period under consideration is in the order of 1500-1800 mm/y, in contrast to the values in the deserts east and south, where the evaporation is less than 20 mm/y. Observed annual evaporation of this lake is known to be about 1500 mm and to vary with the salinity at the surface of the lake and freshening by the water inflow (Dayan and Morin 2006; Hamdani et al. 2018). Over land, higher evaporation is seen over the Judean Mountains and the Jordanian Highlands. High correlation with the orography and soil types is seen (Figure 1). Evaporation is probably correlated with rainfall which in turn is correlated with topography. Particularly, in the Jordanian Highlands where maximum evaporation is around 200 mm/y, the complex topography coincides with sandy loam soils, whereas most of the soil in study region is defined as loamy clay or clay (Figure 1). The evaporative difference field between simulations in Figure 5a shows a highly inhomogeneous patchiness not evidencing any relationship with orography or soil type,

but rather with changes in the precipitation pattern in the SEN^{CLIM} simulation as seen in Figure 5b.

In agreement with the temporal series of areal mean precipitation in Figure 3 higher annual precipitation are in the north-west and -east, with respect to the southern regions. Topographic features exert a large impact on precipitation distribution with maxima of about 175 to 300 mm/y over the Judean Mountains and the Jordanian Highlands. To the northern end of the Dead Sea valley, the largest precipitation difference between the REF^{CLIM} and the SEN^{CLIM} simulations is identified, rather than directly over the Dead Sea area noting the importance of advected moisture from the Dead Sea evaporative flux upslope and along the Dead Sea valley as well as the indirect effects of a different spatial distribution of low-tropospheric water vapour in the occurrence of precipitating convection.

Regarding the impact on the large-scale conditions, differences in the spatial pattern and strength of the 500 hPa geopotential height field are identified over the Dead Sea (not shown). In the 10-year mean, differences up to 0.002gpdm higher in SEN than in REF are observed. Around the Dead Sea area, the differences are smaller and more irregular. Generally, the differences are higher in the east of the Dead Sea than in the west.

Precipitation probability distribution function

While the probability for lower intensity precipitation is very similar in the REF^{CLIM} and the SEN^{CLIM} simulations differences are recognized in the higher precipitation intensities, from about 150 mm/d (Figure 6a). Particularly, above 180 mm/d extreme precipitation values occur less frequent at the SEN^{CLIM} simulation where a drier, warmer and more stable atmosphere is identified (Figure 2).

SAL

The use of the SAL method in this study differs from the approach frequently presented in literature since it is here not our purpose to examine differences between the simulated field and observations (adequate observations for this comparison are not available in the area), but to compare changes regarding the structure, amount and location of the precipitation field between our reference and sensitivity experiments. Figure 6b shows that when the mean precipitation over the whole simulation period is considered all three SAL components are close to zero, meaning that very small differences are found. However, when single precipitation events in the REF^{CLIM} simulation are compared with the same period at the SEN^{CLIM} simulation, larger

differences regarding structure, amount and location of rainfall events are found. For further examination of this issue two exemplary heavy precipitation events (indicated by boxes in Figure 6b) are analysed in detail. In both cases, a negative A-component is recognized, that is, less precipitation falls in the SEN^{CLIM} simulation. The S-component also evidences the change in the structure of the convective cells. The L-component is low meaning that the convective location does not change significantly in the SEN^{CLIM} simulation, in contrast to the intensity and structure of the cells.

3.2 Sensitivity of atmospheric conditions to the Dead Sea drying: episodic investigation

Among those events exhibiting differences in the precipitation field between both simulations (Table 1 and Figure 6b) two situations occurring in the time period of the 14 to 19 November 2011 are investigated in the following.

In this term, the synoptic situation is characterized by a Cyprus low and its frontal system located over the Dead Sea at about 00 UTC on the 15 November 2011 and at 12 UTC on the 18 November 2011. The low-pressure system and its frontal system induced strong south-westerly to westerly winds with mean wind velocities up to 15 m/s.

In the first situation (hereafter CASE1), in association with the western movement of the cold front a convective system develops over the Jordanian Highlands with precipitation starting at about 21 UTC on the 14 November 2011. This convective system is of high interest because of the large difference in its development between the $REF^{14.11}$ and the $SEN^{14.11}$ simulations.

In Figure 7a the 24-h accumulated precipitation, from 14.11 09 UTC to 15.11 08 UTC, in the investigation area is shown for the $REF^{14.11}$ and the $SEN^{14.11}$ simulations. Two precipitation areas are seen, on the north-western and north-eastern of the Dead Sea. Larger difference between models is on the north-eastern region (24-h accumulated precipitation > 100 mm/d in $REF^{14.11}$, while < 50 mm/d in $SEN^{14.11}$), which is the focus of our analysis.

The $REF^{14.11}$ simulation shows that in the 6 hours period prior to the initiation of convection the pre-convective atmosphere and more specifically the lower boundary layer exhibit a moist (IWV ~ 24-30 mm, qvPBLmax ~ 7-10 g/kg) and unstable (CAPE ~ 1100 J/kg; KO-index ~ -8 K; not shown) air mass on the western side of the

investigation area, particularly close to the western Mediterranean coast, and drier (IWV~ 8-16; qvPBLmax ~ 4-6 g/kg) and more stable conditions (CAPE< 200 J/kg; KO-index ~ 0-2 K) on the eastern side of the domain (Figure 7b). A maximum difference of about 5 g/kg from west to east is established in the lower boundary layer.

Main differences between both simulations are over the Dead Sea (IWV difference up to 2 mm and qvPBL up to 1.5 g/kg) and north and north-east of it, but almost similar conditions everywhere else. In our target area (subdomain of investigation where the convection episode takes place (red box in Figure 7)), north-east of the Dead Sea, a drier and a more stable atmosphere is identified at the $SEN^{14.11}$ simulation.

The evolution of the wind circulation systems in the area is similar in both simulations (Figure 7c). The 700 hPa, 850 and 950 hPa winds dominantly blow from the south south-west during the pre-convective environment advecting the moist unstable air mass towards the Dead Sea valley and north-east of it, directly affecting the atmospheric conditions at the target area (for a comparison with a climatology of the wind conditions in the region please see Metzger et al. 2017). In both simulations, the passage of the cold front over the Dead Sea establishes a strong southerly wind from about 10 UTC on the 14 November 2011.

Prior to this time, dry air was advected below about 850 hPa towards the target area from the east. The turning of the low-level winds and the resulting moistening of the atmosphere is well and equally captured by both simulations (Figure 8a). Furthermore, at the near-surface, from about 16 UTC, ~ 5 h prior to convection initiation in the target area, a near-surface convergence line forms at the foothills of the northern part of the Jordanian Highlands, which is also well and equally captured by both simulations (Figure 8b). The lifting provided by the convergence line triggers convection in the area. However, the drier and more stable atmosphere in the $SEN^{14.11}$ simulation results in less intense convection, weaker updrafts, and reduced precipitation at the eastern slope of the valley.

In the second case, CASE2, we address an episode of localized convection taking place on the north-western edge of the Dead Sea in the REF simulation, whereas no convection develops in the SEN simulation. The isolated convection in the REF simulation left about 50 mm rain in 3 h starting at about 03 UTC on the 19 November 2011 (Figure 9).

In contrast to CASE1, the modification of the pre-convective environment relevant for convective initiation is in this case dominated by dynamical changes in the mesoscale circulations. Differences in the evolution and strength of the Mediterranean Sea Breeze

(MSB), the Dead Sea breeze and orographic winds influence atmospheric conditions in the target area leading to the assistance to or to the absence of convection. The most significant difference observed between the simulations is in the development of a strong near-surface convergence line in the REF simulation (which is not present in the SEN simulation hindering convection in the area), which forms about 2 h before convective initiation (Figure 10).

Even in the first hours of the 18 November 2011 differences in the speed and direction of the near-surface winds over the Dead Sea and on the eastern flank of the Jordanian Highlands could be identified. A fundamental difference between simulations occurs from about 17 UTC when strong westerly winds indicating the arrival of the MSB reach the western shore of the Dead Sea. One hour later, in the $REF^{19.11}$ run the MSB strongly penetrates the Dead Sea valley reaching as far as the eastern coast in the centre to south areas. However, in the $SEN^{19.11}$ simulation the MSB does not penetrate downward, instead strong northerly winds flow along the valley (Figure 10a). Numerous observational and numerical studies carried out to investigate the dynamics of the MSB (e.g. Naor et al. 2017; Vuellers et al. 2018) showed that the downward penetration of the MSB results from temperature differences between the valley air mass, which is warmer than the maritime air mass. An examination of temperature differences along a near-surface north-south valley transect (positions in Figure 10a) indicates a decrease of about 4 ºC at the near-surface over the dried Dead Sea area in contrast to negligible changes on a parallel transect inland, on the western coast of the Dead Sea. These evidences the notorious impact of the absence of water in the valley temperature, thus, gradients in the region. The colder valley temperatures do not favour the downward penetration of the MSB, which strongly affects the atmospheric conditions in the valley. Moreover, a north-easterly land breeze is visible from about 20 UTC on the eastern shore of the Dead Sea in the $REF^{19.11}$ simulation, but not in the $SEN^{19.11}$ simulation (Figure 10b). This situation reflects an interesting case different from the ones generally presented in former investigations in the area (e.g. Alpert et al. 1997 ; and Alpert et al. 2006b) in which due to the recent weakening of the Dead-Sea breeze, mainly because of the drying and shrinking of the Sea, the Mediterranean breeze penetrates stronger and earlier into the Dead-Sea Valley increasing the evaporation because of the strong, hot and dry wind.

Mountain downslope winds develop in both simulations from about 22 UTC. One hour later, strong northerly valley flow in the northern part of the Dead Sea contrasts with the westerly flow in the $SEN^{19.11}$ simulation (Figure 10c). As the valley cools down during night time in the SEN simulation, T2m decreases about 1 K from 20 UTC to 03 UTC in

522 contrast with the 0.1 K decrease of the Dead Sea in the REF simulation, the
523 temperature gradient weakens and the northerly valley flow present in the REF
524 simulation is absent in the SEN simulation. During the night, the synoptic conditions
525 gain more influence than the local wind systems governing the conditions in the valley
526 during day time. South-easterly winds prevail in the valley in both simulations. Much
527 stronger wind velocities are reached in the REF simulation, confirming the sensitivity of
528 large-scale dynamics to near-surface climate change-induced impacts.

529 The encounter of the north north-westerly and south south-easterly winds over the
530 Dead Sea area in the $REF^{19.11}$ simulation induces the formation of a convergence zone,
531 which intensifies and extends offshore over the next hours and determines the location
532 of convective initiation. Meanwhile, homogeneous south-easterly winds are observed in
533 the SEN simulation (Figure 10d).

534 The differences in the wind circulations contribute to a different distribution of the
535 atmospheric conditions in the target area, particularly, low-tropospheric water vapour
536 as seen in the vertical cross sections in Figure 11. The evolution of the atmospheric
537 conditions in the 3-h period prior to convective initiation evidences the deeper and
538 wetter boundary layer in the $REF^{19.11}$ simulation at the north-western foothills of the
539 ridge at the Jordanian Highlands. Differences of IWV up to 2 mm, and of instability
540 (CAPE) close to 200 J/kg are found in this area (not shown). This is the location of the
541 convergence line where convective updrafts, which start close to the ground, are
542 triggered reaching a maximum vertical velocity of about 5 m/s above the convergence
543 zone in the $REF^{19.11}$ simulation.

544

545 **4. Conclusions**

546 The drying and shrinking of the Dead Sea has been extensively investigated in the last
547 decades from different points of view. This process has been related to significant local
548 climate changes which affect the Dead Sea valley and neighboring regions. The
549 climate of the Dead Sea is very hot and dry. But occasionally the Dead Sea basin is
550 affected by severe convection generating heavy precipitation, which could lead to
551 devastating flash floods.

552 In this study, high-resolution COSMO model simulations are used to assess the impact
553 of the Dead Sea on the occurrence of convective precipitation in the region. A set of
554 high-resolution, ~ 2.8 km, climate simulations covering the period 2003 to 2013, and
555 several numerical weather prediction (NWP) runs on an event time scale (~ 48-36 h)

556 are performed over the Dead Sea area. On a decadal time scale, two simulations are
557 carried out. The first “reference” run with the Dead Sea area, and a second run
558 “sensitivity” in which the Dead Sea is dried out and set to bare soil. The NWP
559 simulations focus on two heavy precipitation events exhibiting relevant differences
560 between the reference and the sensitivity decadal runs. A total of four simulations are
561 performed in this case.

562 As the energy balance partitioning of the Earth’s surface changes due to the drying of
563 the Dead Sea, relevant impacts could be identified in the region. From a climatological
564 point of view, in a future regional climate under ongoing Dead Sea level decline, less
565 evaporation, higher air temperatures and less precipitation is to expect. Reduced
566 evaporation over the Dead Sea occurs from May to October. The cooling effect of
567 evaporation in the neighboring areas results in an increase of T-2m in the absence of
568 the Dead Sea. Atmospheric conditions, such as air temperature and humidity, are
569 mostly affected in the lower-tropospheric levels, which in turn influence atmospheric
570 stability conditions, hence, precipitating convection. In general, the number of dry/wet
571 days is not largely affected by the drying of the Dead Sea, although these differences
572 could be larger for hourly precipitation; rather the structure and intensity of the heavier
573 precipitation events is changed. While a general and homogeneous decrease in
574 evaporation is seen at the SEN^{CLIM} simulation, precipitation deviations occur in both
575 directions, which could suggest and impact on the timing of the events. A relevant year
576 to year variability is observed in evaporation-precipitation which indicates the need of
577 long time series of observations to understand local conditions and to validate model
578 simulations.

579 The detailed analysis of two heavy precipitation events allowed us to further assess the
580 possible causes and the processes involved regarding the decrease in precipitation
581 intensity or the total omission of convection with respect to the reference simulation in
582 the absence of the Dead Sea water. Two main components, strongly affected by the
583 drying of the Dead Sea, are found to be highly relevant for the understanding of the
584 environmental processes in the Dead Sea region.

585 (a) First, the lower-atmospheric boundary layer conditions. Changes in the energy
586 balance affect the atmosphere through the heat exchange and moisture supply. The
587 drying of the Dead Sea in the SEN simulations and the resulting decrease in local
588 evaporation, impact the Dead Sea Basin conditions and the neighbouring areas. A
589 reduction in boundary layer humidity and an increase in temperature result in a general
590 decrease of atmospheric instability and weaker updrafts indicating reduced deep-

591 convective activity. Main differences on the atmospheric conditions are directly over the
592 Dead Sea, but these conditions are frequently advected to neighbouring areas by the
593 thermally driven wind systems in the region which play a key role for the redistribution
594 of these conditions and the initiation of convection.

595 (b) Secondly, wind systems in the valley. In the arid region of the Dead Sea Basin with
596 varied topography, thermally and dynamically driven wind systems are key features of
597 the local climate. Three different scales of climatic phenomena coexist: The
598 Mediterranean Sea Breeze (MSB), the Dead Sea breeze and the orographic winds,
599 valley-, and slope-winds, which are known to temper the climate in the Dead Sea valley
600 (Shafir and Alpert, 2011). The drying of the Dead Sea in the SEN simulation disturbs
601 the Dead Sea thermally driven wind circulations. The Dead Sea breezes are missing,
602 weaker wind speeds characterize the region and along valley winds are consequently
603 affected. Furthermore, the dynamics of the Mediterranean breeze penetration into the
604 Jordan Valley are affected.
605
606 Consequently, the impacts on convection initiation and development are twofold:
607 (i) Distinct redistribution of atmospheric conditions, locally or remotely, which yields to
608 different atmospheric conditions that in the absence of the Dead Sea result in a
609 reduced moisture availability in the lower atmospheric levels and increased stability
610 hindering convection or reducing the intensity of the events.
611 (ii) Modification of the divergence/convergence field. The absence of the Dead Sea
612 substantially modifies the wind circulation systems over the Dead Sea valley, which
613 leads to the omission of convergence lines which act as triggering mechanism for
614 convection.
615
616 We can conclude that in general the lack of sufficient low-atmospheric moisture in
617 relation to the drying of the Dead Sea, the increase of atmospheric stability in addition
618 to an absence or reduction in the intensity of the convergence zones, works against
619 initiation or intensification of precipitating convection in the area. The relevance of the
620 small-scale variability of moisture and the correct definition and location of
621 convergence lines for an accurate representation of convective initiation illustrates the
622 limitation and the lack of adequate observational networks in the area and the need for
623 high-resolution model simulations of boundary layer processes to predict intense and
624 localised convection in the region.

625 These results contribute to gain a better understanding of expected conditions in the
626 Dead Sea valley and neighbouring areas under continual lake level decline. Energy

balance partitioning and wind circulation systems are determinant for local climatic conditions, e.g. temperature and humidity fields as well as aerosol redistribution, therefore, any change should be well understood and properly represented in model simulations of the region. Our results point out, in agreement with past modelling activities in the region, the need to further improve the representation of precipitation fields in the area, particularly close to the Mediterranean coastline. More accurate Mediterranean SST input fields have been suggested as relevant to reduce the model inaccuracies. Furthermore, a more realistic representation of the lake shape, water salinity and temperature, as well as Dead Sea abundance must be addressed to accurately describe the impact on the simulation results. In a further step, the authors will investigate some of these issues performing sensitivity experiments, and will assess the impact of model grid resolution on the horizontal and vertical flow field in the region across scales, including the impact on large-scale dynamics. We will also put emphasis in trying to better understand the dynamics of the MSB under lake level decline using high-resolution modelling, especially the contrasting behaviour pointed out in this study. Fine resolution simulations up to 100 m will be performed for this purpose. Furthermore, we will provide a verification of the complex chain of processes in the area using unique measurements in the framework of the interdisciplinary virtual institute Dead Sea Research VEnue (DESERVE; Kottmeier et al., 2016).

Author contribution

SK wrote the manuscript, analysed the data, interpreted the results and supervised the work. JH carried out data analysis, interpretation of results and prepared all the figures.

Acknowledgements

The first author's research was supported by the Bundesministerium für Bildung und Forschung (BMBF; German Federal Ministry of Education and Research). The authors acknowledge the colleagues at the Karlsruhe Institute of Technology (KIT) involved in the interdisciplinary virtual institute Dead Sea Research VEnue (DESERVE) for their support and interesting discussions. We acknowledge Sebastian Helgert and Alberto Caldas Alvarez for their assistance in the preparation of the simulations. This article is a contribution to the HyMeX program.

References

Alpert, P., and Shay-EL, Y.,: The Moisture Source for the Winter Cyclones in the Eastern Mediterranean. Israel Meteorological Research Papers, 5, 20-27, 1994.

Alpert, P., and Coauthors: Relations between climate variability in the Mediterranean region and the tropics: ENSO, South Asian and African monsoons, hurricanes and Saharan dust. Developments in Earth and Environmental Sciences, 4, 149-177, https://doi.org/10.1016/S1571-9197(06)80005-4, 2006.

Alpert, P., Shafir, H., and Issahary, D.,: Recent Changes in the Climate At the Dead Sea – a Preliminary Study. Climatic Change, 37(3), 513-537, https://doi.org/10.1023/A:1005330908974, 1997.

Andersson, T., Andersson, M., Jacobsson, C., Nilsson, S.: Thermodynamic indices for forecasting thunderstorms in southern Sweden. Meteorol. Mag. 116, 141-146, 1989.

Arkin, Y., and Gilat, A.: Dead Sea sinkholes - an ever-developing hazard. Environmental Geology, 39(7), 711-722, https://doi.org/10.1007/s002540050485, 2000.

Ashbel, D., and Brooks, C.: The influence of the dead sea on the climate of its neighbourhood. Quarterly Journal of the Royal Meteorological Society, 65(280), 185-194, https://doi.org/10.1002/qj.49706528005, 1939.

Ban, N., Schmidli, J., and Schär, C.: Evaluation of the convection-resolving regional climate modeling approach in decade-long simulations, J. Geophys. Res. Atmos., 119, 7889– 7907, https://doi.org/10.1002/2014JD021478, 2014.

Belachsen, I., Marra, F., Peleg, N., and Morin, E.: Convective rainfall in dry climate: relations with synoptic systems and flash-flood generation in the Dead Sea region. Hydrology and Earth System Sciences Discussions, 21, 5165-5180, https://doi.org/10.5194/hess-21-5165-2017, 2017.

Böhm, U., and Coauthors: The Climate Version of LM: Brief Description and Long-Term Applications. COSMO Newsletter, 6, 225-235, 2006.

Businger, J., Wyngaard, J., Izumi, Y., and Bradley, E.: Flux-Profile Relationships in the Atmospheric Surface Layer. Journal of the Atmospheric Sciences, 28(2), 181-189, https://doi.org/10.1175/1520-0469(1971)028<0181:FPRITA>2.0.CO;2, 1971.

692 Byun, H., and Kim, D.: Comparing the Effective Drought Index and the Standardized
693 Precipitation Index. Options Méditerranéennes. Séries A. Mediterranean
694 Seminars, 95, 85-89, 2010.

695 Byun, H., and Wilhite, D.: Objective quantification of drought severity and duration. J.
696 Climate, 12(9), 2747-2756, https://doi.org/10.1175/1520-
697 0442(1999)012<2747:OQODSA>2.0.CO;2, 1999.

698 Cohen, S., and Stanhill, G.: Contemporary Climate Change in the Jordan Valley. J.
699 Appl. Meteor., 35(7), 1051-1058, https://doi.org/10.1175/1520-
700 0450(1996)035<1051:CCCITJ>2.0.CO;2, 1996.

701 Corsmeier, U., Behrendt, R., Drobinski, P., Kottmeier, C.: The mistral and its
702 effect on air pollution transport and vertical mixing, Atmos. Res., 74, 275–302,
703 https://doi.org/https://doi.org/10.1016/j.atmosres.2004.04.010, 2005.

704 Dayan, U., and Morin, E.: Flash flood – producing rainstorms over the Dead Sea: A
705 review. Geological Society of America, 401(4), 53-62,
706 https://doi.org/10.1130/2006.2401(04) , 2006.

707 Dayan, U., and Sharon, D.: Meteorological parameters for discriminating between
708 widespread and spotty storms in the Negev. Israel Journal of Earth Sciences,
709 29(4), 253-256, 1980.

710 Dayan, U., Ziv, B., Margalit, A., Morin, E., and Sharon, D.: A severe autumn storm over
711 the middle-east: synoptic and mesoscale convection analysis. Theoretical and
712 Applied Climatology, 69(1-2), 103-122, https://doi.org/10.1007/s007040170038,
713 2001.

714 Doms, G., and Baldauf, M.: A Description of the Nonhydrostatic Regional COSMO-
715 Model. Part I: Dynamics and Numerics. Deutscher Wetterdienst, 2015.

716 Doswell, C., and Rasmussen, E.: The Effect of Neglecting the Virtual Temperature
717 Correction on CAPE Calculations. Weather and Forecasting, 9(4), 625-629,
718 https://doi.org/10.1175/1520-0434(1994)009<0625:TEONTV>2.0.CO;2, 1994.

719 FAO/IIASA/ISRIC/ISSCAS/JRC.: Harmonized World Soil Database (version 1.2). FAO,
720 Rome, Italy and IIASA, Laxenburg, Austria, (accessed 01.02.2017) , 2009.

721 Fosser, G., Khodayar, S., and Berg, P., 2014: Benefit of convection permitting climate
722 model simulations in the representation of convective precipitation, Clim. Dyn.,
723 44(1– 2), 45– 60.

724 Gavrieli, I., Bein, A., and Oren, A., 2005: The expected impact of the “Peace Conduit”
725 project (the Red Sea - Dead Sea pipeline) on the Dead Sea. Mitigation and
726 Adaptation Strategies for Global Change, 10(4), 759-777,
727 https://doi.org/10.1007/s11027-005-5144-z.

728 European Commission, Joint Research Centre, 2003: Global Land Cover 2000
729 database, (accessed 01.02.2017).

730 GLOBE National Geophysical Data Center, 1999: Global Land One-kilometer Base
731 Elevation (GLOBE) v.1. Hastings, D. and P.K. Dunbar. National Geophysical
732 Data Center, NOAA, (accessed 01.02.2017).

733 Greenbaum, N., Ben-Zvi, A., Haviv, I., and Enzel, Y., 2006: The hydrology and
734 paleohydrology of the Dead Sea tributaries. Geological Society of America,
735 401(4), 63-93, https://doi.org/10.1130/2006.2401(05).

736 Haylock, M.R., Hofstra, N., Klein Tank, A.M.G., Klok, E.J., Jones, P.D. and New, M.
737 2008, A European daily high-resolution gridded dataset of surface temperature and
738 precipitation. Journal of Geophysical Research: Atmospheres, 113, D20119.
739 https://doi.org/10.1029/2008JD10201.
740

741 Hochman, A., Mercogliano, P., Alpert, P., Saaroni, H. and Bucchignani, E., 2018. High-
742 resolution projection of climate change and extremity over Israel using COSMO-CLM.
743 International Journal of Climatology, 38(14), pp.5095-5106.
744

745 Houze, R., 2012: Orographic effects on precipitating clouds. Reviews of Geophysics,
746 50(1), https://doi.org/10.1029/2011RG000365.

747 Kalthoff, N., Horlacher, V., Corsmeier, U., Volz-Thomas, A., Kolahgar, B., Geiß, H.,
748 Möllmann-Coers, M., and Knaps, A. 2000: Influence of valley winds on transport
749 and dispersion of airborne pollutants in the Freiburg-Schauinsland area, J.
750 Geophys. Res. Atmos, 105, 1585–1597, https://doi.org/10.1029/1999jd900999.
751

752 Khodayar, S., Kalthoff, N., and Schaedler, G., 2013: The impact of soil moisture
753 variability on seasonal convective precipitation simulations. Part I: validation,
754 feedbacks, and realistic initialisation. Meteorologische Zeitschrift, 22(4), 489-505,
755 https://doi.org/10.1127/0941-2948/2013/0403.

Kunin, P., Alpert, P. and Rostkier-Edelstein, D., 2019. Investigation of sea-breeze/foehn in the Dead Sea valley employing high resolution WRF and observations. Atmospheric Research.

Lensky, N. and Dente, E., 2015. The hydrological proecesses driving the accelerated Dead Sea level decline in the past decades. Geological Survey of Israel Report.

Llasat, M., and Coauthors, 2010: High-impact floods and flash floods in Mediterranean countries: the FLASH preliminary database. Advances in Geosciences, 23, 47-55, https://doi.org/10.5194/adgeo-23-47-2010.

Metzger, J., Nied, M., Corsmeier, U., Kleffmann, J., and Kottmeier, C., 2017: Dead Sea evaporation by eddy covariance measurements versus aerodynamic, energy budget, Priestley-Taylor, and Penman estimates. Hydrology and Earth System Sciences Discussions, 22(2), 1135-1155, https://doi.org/10.5194/hess-2017-187.

Miglietta MM, Conte D, Mannarini G, Lacorata G, Rotunno R. 2011. Numerical analysis of a Mediterranean 'hurricane' over south-eastern Italy: sensitivity experiments to sea surface temperature. *Atmos. Res.* **101**: 412–426.

Moncrieff, M., and Miller, M., 1976: The dynamics and simulation of tropical cumulonimbus and squall lines. Quarterly Journal of the Royal Meteorological Society, 102(432), 373-394, https://doi.org/10.1002/qj.49710243208, 2014.

Naor, R., Potchter, O., Shafir, H., and Alpert, P.: An observational study of the summer Mediterranean Sea breeze front penetration into the complex topography of the Jordan Rift Valley, Theor. Appl. Climatol., 127, 275–284, https://doi.org/10.1007/s00704-015-1635-3, 2017.

Prein, A., Gobiet, A., Suklitsch, M., Truhetz, H., Awan, N., Keuler, K., and Georgievski, G. : Added value of convection permitting seasonal simulations, Clim. Dyn., 41(9– 10), 2655– 2677, 2013.

Ritter, B., and J.-F. Geleyn, 1992. A comprehensive radiation scheme for numerical weather prediction models with potential applications in climate simulations. Mon. Wea. Rev., 120, 303–325.

Rostkier-Edelstein, D., Liu, Y., Wu, W., Kunin, P., Givati, A. and Ge, M., 2014. Towards a high-resolution climatography of seasonal precipitation over Israel. International Journal of Climatology, 34(6), pp.1964-1979.

Schaedler, G., and Sasse, R.: Analysis of the connection between precipitation and synoptic scale processes in the Eastern Mediterranean using self-organizing maps. Meteorologische Zeitschrift, 15(3), 273-278, https://doi.org/10.1127/0941-2948/2006/0105, 2006.

Shafir, H., and Alpert, P.: Regional and local climatic effects on the Dead-Sea evaporation. Climatic Change, 105(3-4), 455-468, https://doi.org/10.1007/s10584-010-9892-8, 2011.

Sharon, D., and Kutiel, H.: The distribution of rainfall intensity in Israel, its regional and seasonal variations and its climatological evaluation. International Journal of Climatology, 6(3), 277-291, https://doi.org/10.1002/joc.3370060304, 1986.

Smiatek, G., Kunstmann, H., and Heckl, A.: High-resolution climate change simulations for the Jordan River area. Journal of Geophysical Research, 116(D16), https://doi.org/10.1029/2010JD015313, 2011.

Stanhill, G.: Changes in the rate of evaporation from the dead sea. International Journal of Climatology, 14(4), 465-471, https://doi.org/10.1002/joc.3370140409,1994.

Vicente-Serrano, S., Beguería, S., López-Moreno, J.: A Multiscalar Drought Index Sensitive to Global Warming: The Standardized Precipitation Evapotranspiration Index. J. Climate, 23(7), 1696-1718, https://doi.org/10.1175/2009JCLI2909.1, 2010.

Vüllers, J., Mayr, G. J., Corsmeier, U., and Kottmeier, C.: Characteristics and evolution of diurnal foehn events in the Dead Sea valley. Atmos. Chem. Phys., 18, 18169-18186, https://doi.org/10.5194/acp-18-18169-2018, 20, 2018.

Wernli H, Paulat M, Hagen M, Frei C. SAL – a novel quality measure for the verification of quantitative precipitation forecasts. Mon. Weather Rev. 136: 4470–4487, 2008.

Yatagai, A., Alpert, P. and Xie, P. (2008) Development of a daily gridded precipitation data set for the Middle East. Advances in Geosciences, 12, 1–6.

Yatagai, A., Kamiguchi, K., Arakawa, O., Hamada, A., Yasutomi, N. and Kitoh, A., 2012: APHRODITE: constructing a long-term daily gridded precipitation dataset for Asia based on a dense network of rain gauges. Bulletin of the American Meteorological Society, 93, 1401–1415.

Tables

	PREC $_{diffmn}$	REF $_{PMX}$	SEN $_{PMX}$	PREC relative diff [%]	Synoptic Situation	REF $_{CAPEmx}$	SEN $_{CAPEmx}$	REF $_{KOmn}$	SEN $_{KOmn}$	Localised/ Widespread (Subarea affected)
08.12.2004	0,10	30,09	31,31	2,76	ARST	1	1	4,85	4,85	W (A1, A2)
13.01.2006	-0,11	45,64	54,64	-4,26	Cyprus Low	239	225	6,57	6,54	L/W (A1, A3)
16.04.2006	0,11	57,41	56,09	4,89	Syrian Low	43	47	1,97	1,94	L (A1, A4)
10.04.2007	0,29	42,61	70,20	30,78	Cyprus Low	686	679	-4,77	-4,70	L (A2, A4)
13.04.2007	0,12	134,36	127,79	1,62	Cyprus Low	573	576	-1,95	-1,92	L (A1, A2, A3, A4)
12.05.2007	-0,16	41,82	47,90	-8,24	Syrian Low	436	81	-5,30	-5,29	L (A1, A2)
27.01.2008	-0,14	23,11	17,24	-17,25	Syrian Low	7	7	5,12	5,12	W (A1, A3)
25.10.2008	-0,23	139,01	125,73	-16,52	ARST	1274	1361	-5,50	-4,08	L (A3)
13.11.2008	0,30	40,83	45,55	25,68	ARST	25	7	1,37	1,38	L (A2, A4)
14.05.2009	-0,39	59,28	68,84	-8,49	Syrian Low	433	429	-3,90	-3,91	L (A1, A2, A3, A4)
15.05.2009	0,20	49,23	42,28	13,50	Syrian Low	208	203	-2,30	-2,36	L (A1, A2, A3)
31.10.2009	-0,19	166,21	111,79	-7,65	Cyprus Low	435	445	-5,03	-4,46	L (A1, A2)
15.01.2011	0,11	73,02	72,03	3,74	Syrian Low	49	37	7,82	7,83	L/W (A1, A4)
28.05.2011	-0,24	44,51	32,73	-14,33	Cyprus Low	158	170	-10,27	-10,26	W (A2)
15.11.2011	-0,11	42,65	9,34	-65,90	Cyprus Low	2	0	-7,14	-7,12	L (A1, A2)
17.11.2011	0,11	90,07	93,04	4,76	Cyprus Low	386	304	-9,14	-9,16	L (A1)
18.11.2011	-0,11	28,68	34,69	-8,67	Cyprus Low	356	378	-8,61	-8,65	L (A1)
19.11.2011	0,03	58,11	12,36	4,09	Cyprus Low	133	81	-7,60	-7,46	L (A2, A4)
22.10.2012	0,20	29,88	41,64	51,21	ARST	2068	2097	-5,83	-5,59	L (A1, A2)
09.11.2012	-0,11	27,20	22,56	-18,29	Cyprus Low	218	215	3,97	3,98	W (A1)
23.11.2012	-0,21	155,77	117,81	-10,17	ARST	189	286	-2,18	-1,95	L (A1, A2, A3)
25.11.2012	-0,11	41,48	54,33	-7,87	ARST	354	332	4,19	4,37	L (A3, A4)

Table 1: Classification of heavy precipitation cases in the decadal simulation covering the period 2004 to 2013. The areal-mean (study area, Figure 1) difference ($PREC_{diffmn}$) and maximum grid precipitation in the reference (REF_{PMX}) and sensitivity (SEN_{PMX}) realizations, the precipitation relative difference in %, the synoptic situation, and the stability conditions illustrated by maximum grid point CAPE (CAPEmx) and minimum grid point KO-index (KOmn) are summarized. Additionally, the nature of the precipitation, localized (L) or widespread (W) and the main subarea affected (following division in Figure 1; A1, A2, A3, A4) are listed.

Figures

(a)

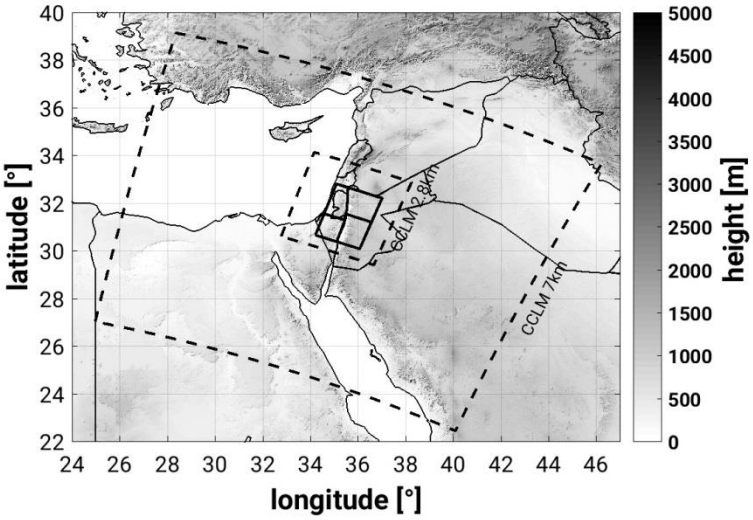

(b)

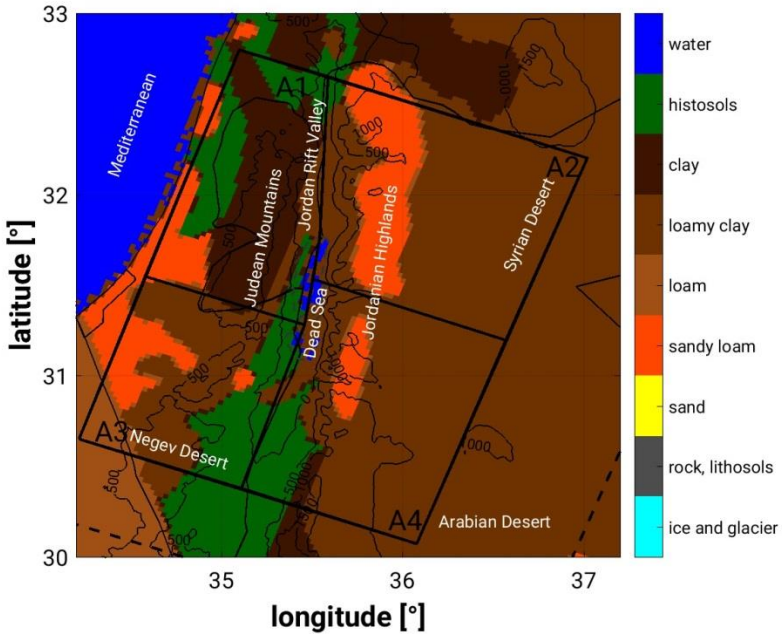

Figure 1: (a) Topography (m above msl), simulation domains (dashed lines, CCLM7km and CCLM2.8km) and study area (bold line). (b) Model soil types (colour scale), topography (black isolines) and study area (black bold line) including the 4 subdomains to be examined, A1-4 (Area 1-4).

(a)

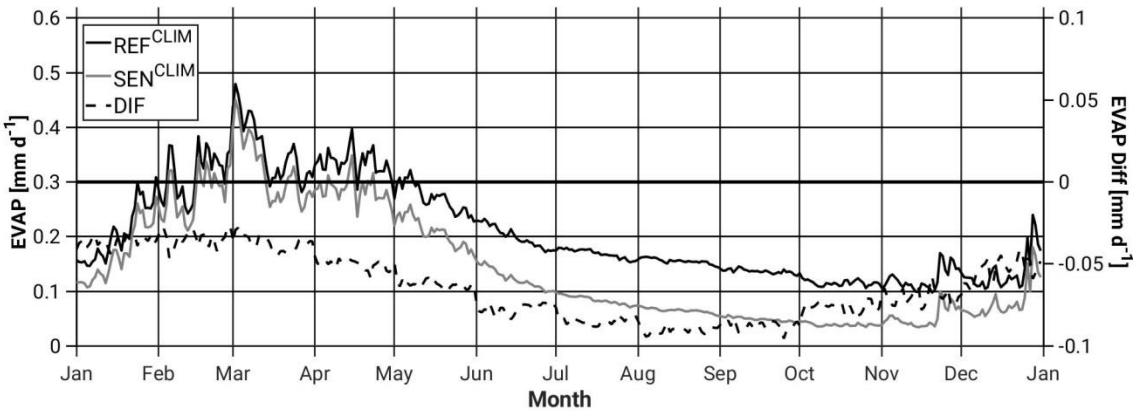
REF^CLIM
SEN^CLIM
DIF
EVAP [mm d-1]
EVAP Diff [mm d-1]
Jan Feb Mar Apr May Jun Jul Aug Sep Oct Nov Dec Jan
Month

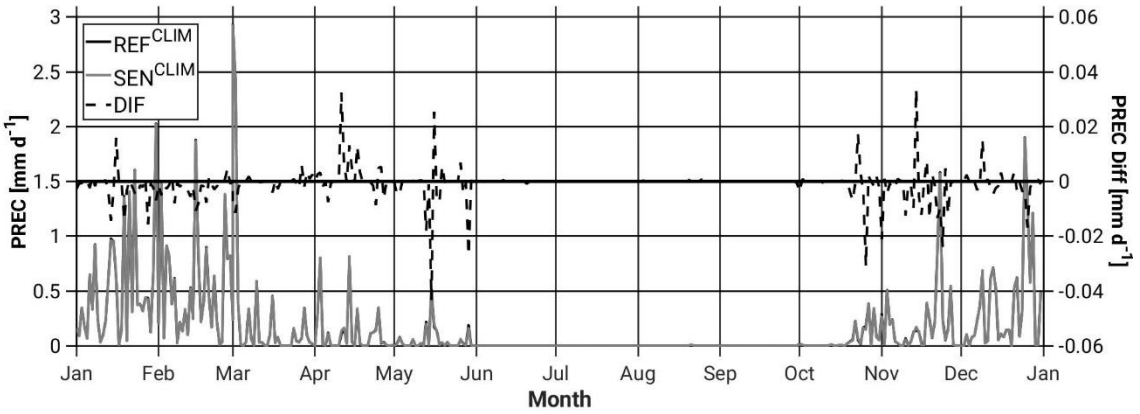
REF^CLIM
SEN^CLIM
DIF
PREC [mm d-1]
PREC Diff [mm d-1]
Jan Feb Mar Apr May Jun Jul Aug Sep Oct Nov Dec Jan
Month

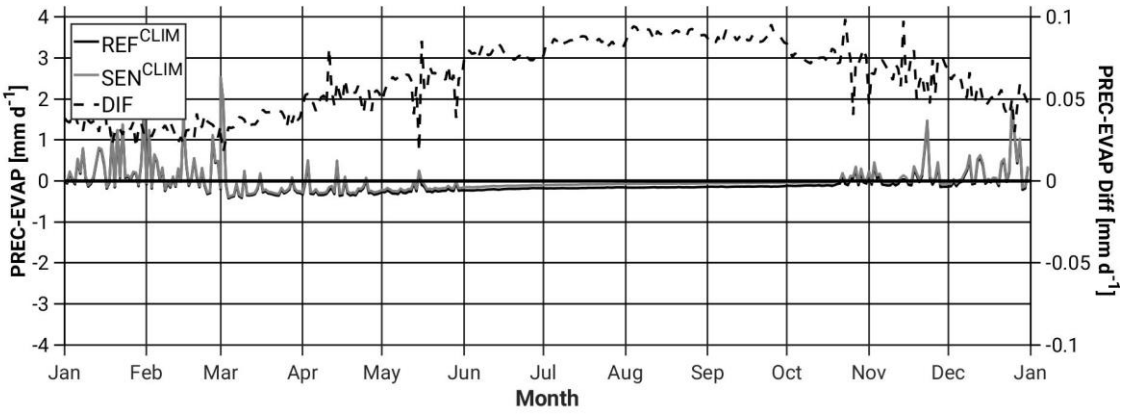
REF^CLIM
SEN^CLIM
DIF
PREC-EVAP [mm d-1]
PREC-EVAP Diff [mm d-1]
Jan Feb Mar Apr May Jun Jul Aug Sep Oct Nov Dec Jan
Month

(b)

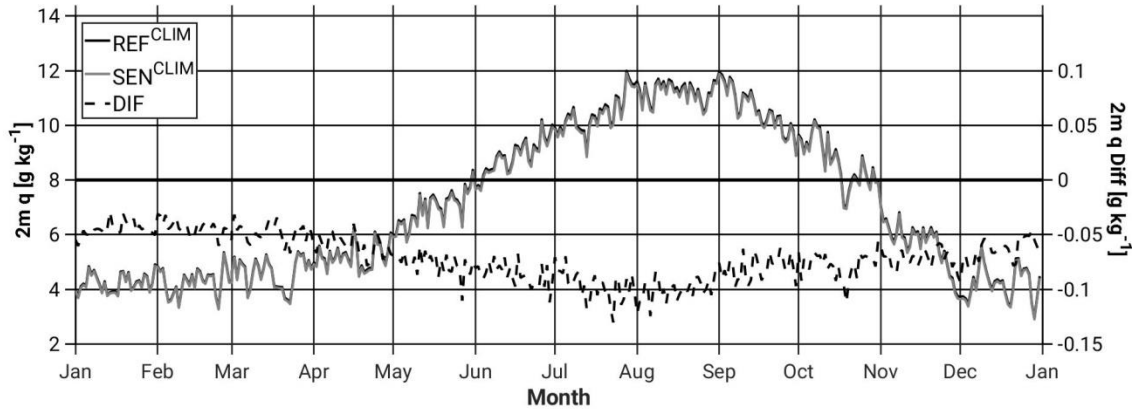
REF^CLIM
SEN^CLIM
DIF
2m q [g kg-1]
2m q Diff [g kg-1]
Jan
Feb
Mar
Apr
May
Jun
Jul
Aug
Sep
Oct
Nov
Dec
Jan
Month

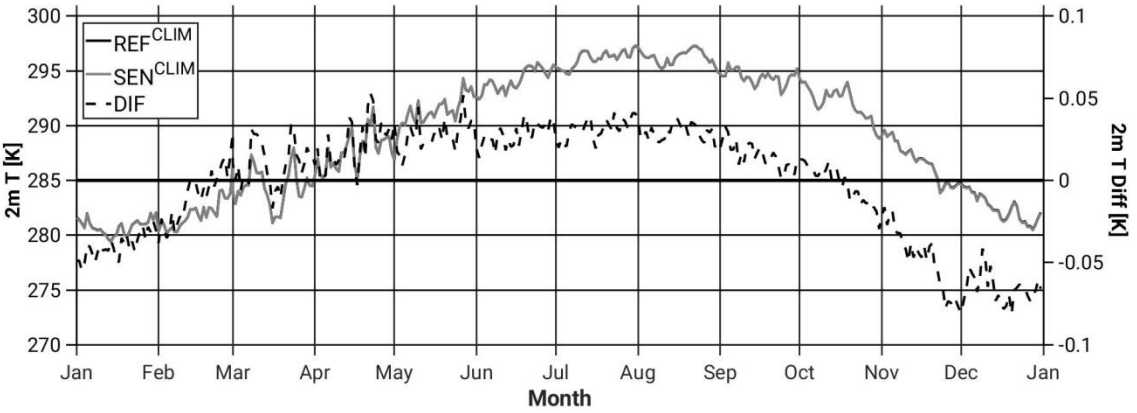
REF^CLIM
SEN^CLIM
DIF
2m T [K]
2m T Diff [K]
Jan
Feb
Mar
Apr
May
Jun
Jul
Aug
Sep
Oct
Nov
Dec
Jan
Month

(c)

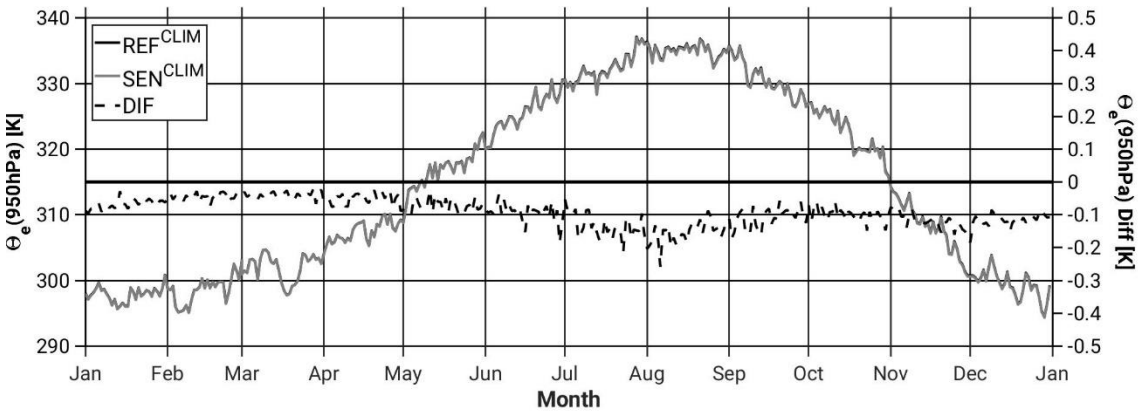
REF^CLIM
SEN^CLIM
DIF
Θe (950hPa) [K]
Θe (950hPa) Diff [K]
Jan
Feb
Mar
Apr
May
Jun
Jul
Aug
Sep
Oct
Nov
Dec
Jan
Month

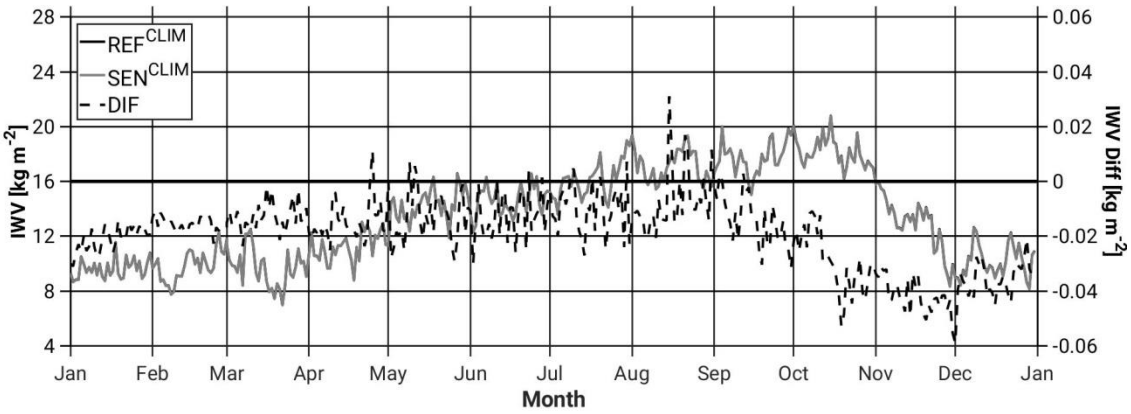
REF^CLIM
SEN^CLIM
DIF
IWV [kg m^-2]
IWV Diff [kg m^-2]
Jan
Feb
Mar
Apr
May
Jun
Jul
Aug
Sep
Oct
Nov
Dec
Jan
Month

(d)

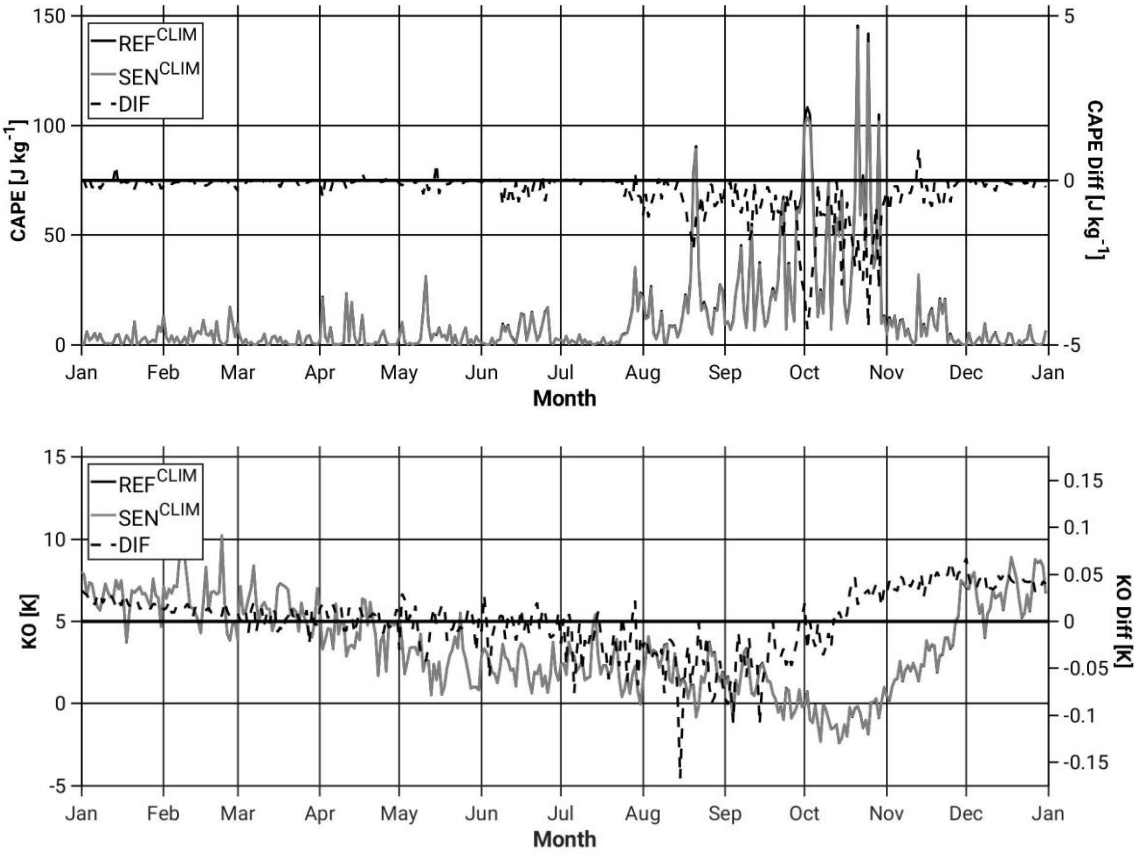

Figure 2: Annual cycle of the areal-daily averaged (and differences (black dashed line; SEN-REF)) of (a) evaporation, precipitation, and precipitation minus evaporation (b) specific humidity and temperature at 2-m, and (c) Θ_e below 950 hPa and IWV, and (d) CAPE and KO-index, from the REF^{CLIM} (full black line) and the SEN^{CLIM} (full grey line) simulations. All grid points in the study area (Figure 1) and the period 2004 to 2013 are considered.

(a)

Area1 (NW) Area2 (NE)

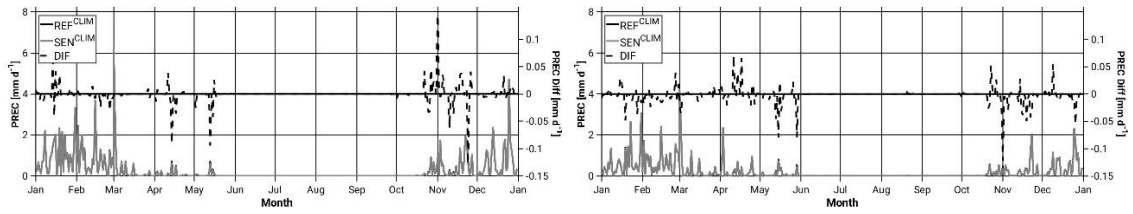

Area3 (SW) Area4 (SE)

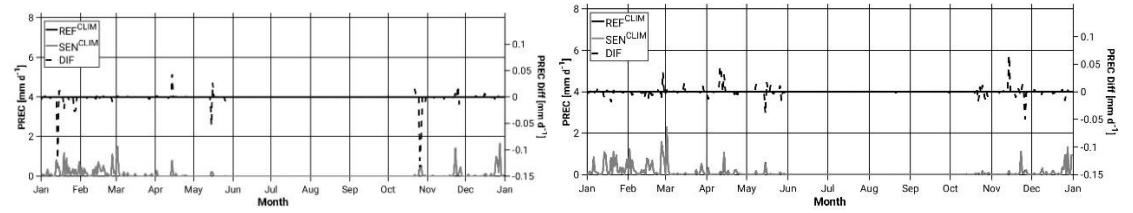

(b)

Area1 (NW) Area2 (NE)

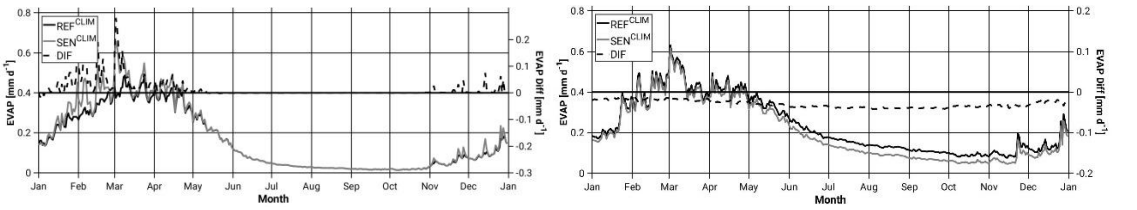

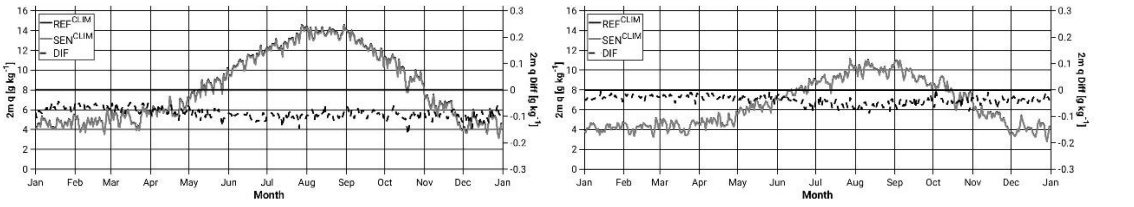

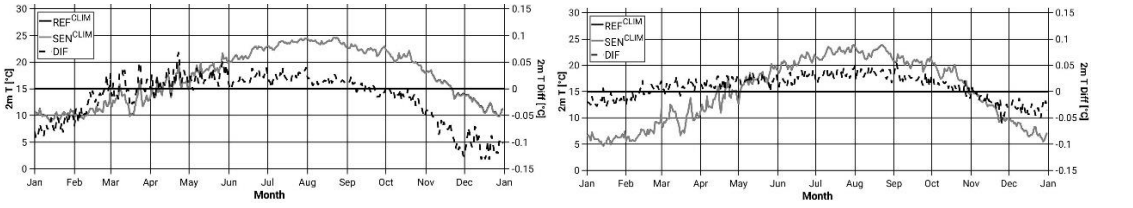

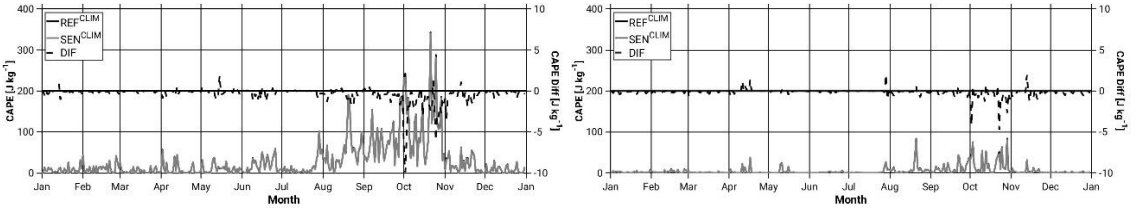

Figure 3: Annual cycle of the areal-daily averaged (and differences (black dashed line; SEN-REF)) of (a) precipitation for areas A1, A2, A3, A4 (see Figure 1b), and (b) evaporation, specific humidity and temperature at 2-m, and CAPE for areas A1 and A2, from the REF^{CLIM} (full black line) and the SEN^{CLIM} (full grey line) simulations. Only land points in the study area (Figure 1) for evaporation, and all grid points for the rest of variables and the period 2004 to 2013 are considered.

(a)

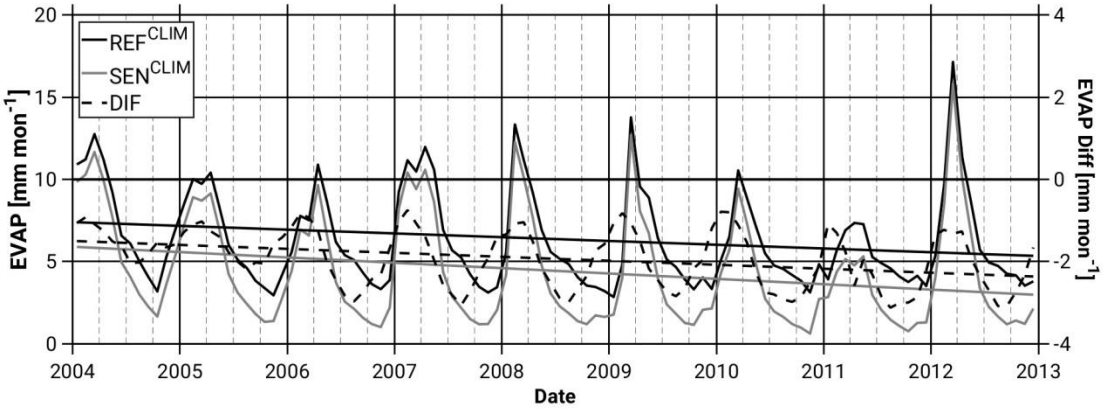

(b)

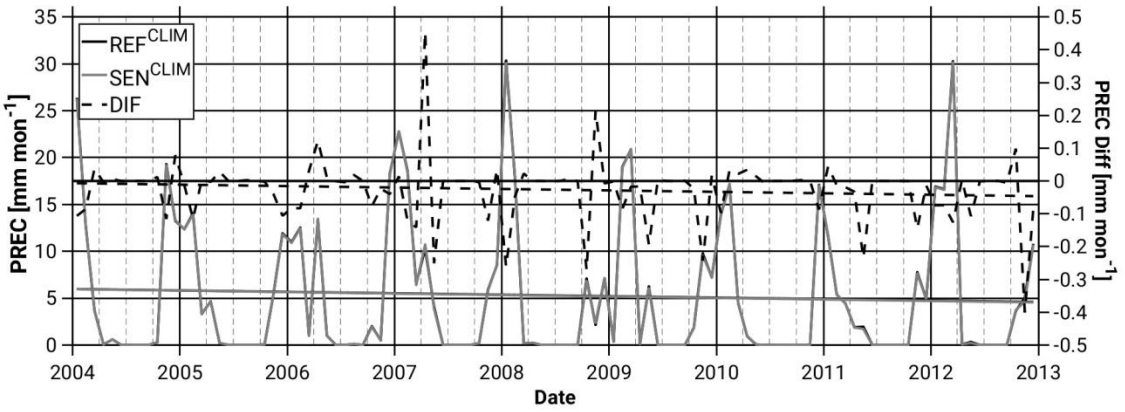

(c)

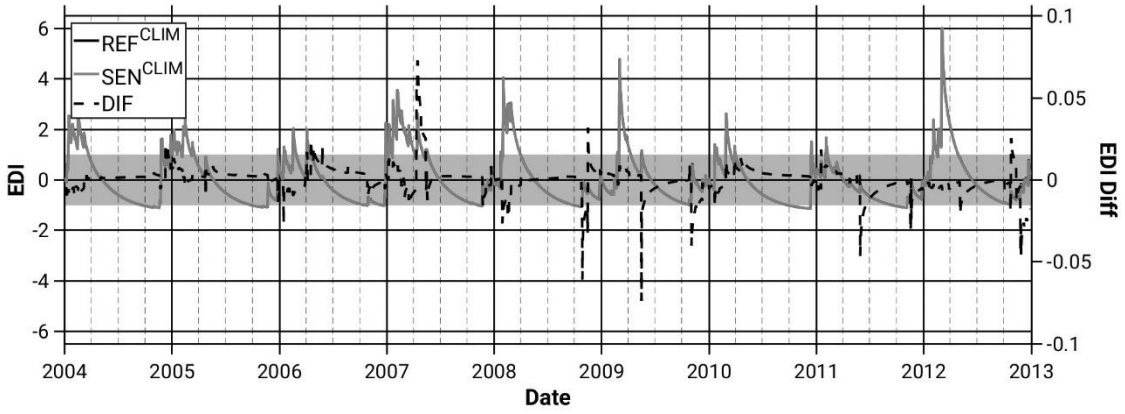

Figure 4: Temporal evolution of the monthly-daily accumulated areal mean values of (a) Evaporation, (b) Precipitation, (c) Effective Drought Index (EDI), from the REF^{CLIM} (full black line) and the SEN^{CLIM} (full grey line) simulations and differences depicted with black dashed lines. The light grey band in (c) indicates the common soil state (-1<EDI<+1). All grid points in the study area (Figure 1) and the period 2004 to 2013 are considered.

(a)

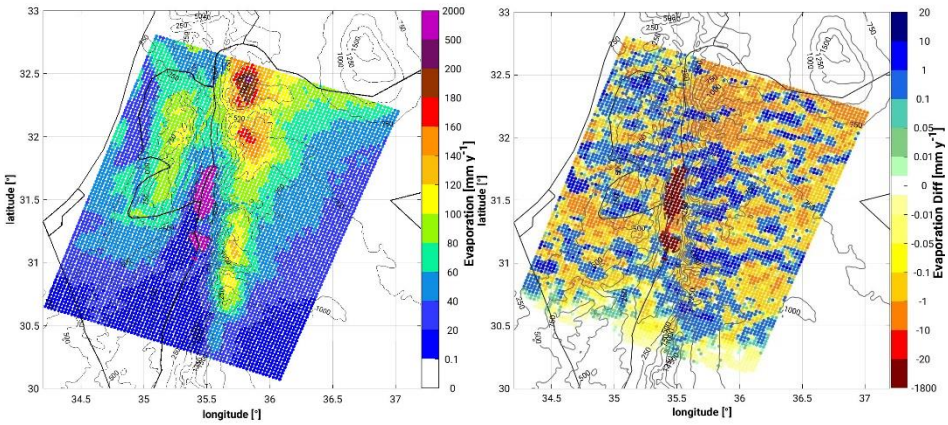

(b)

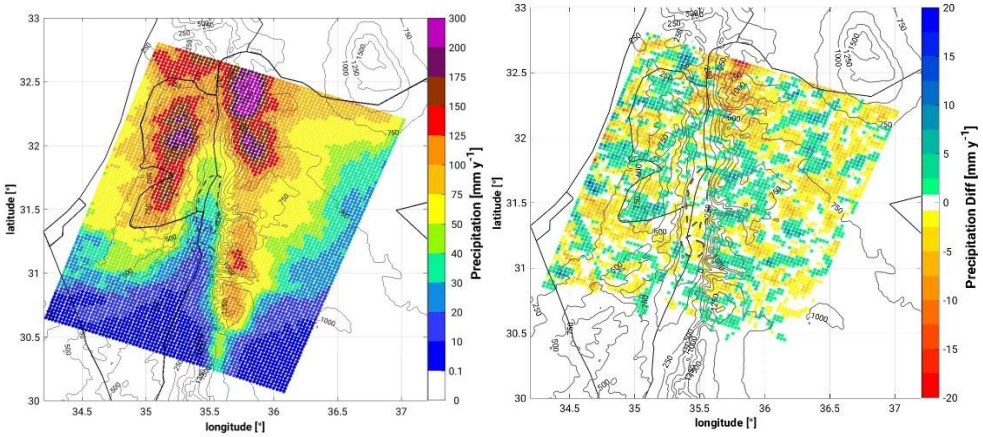

Figure 5: Spatial distribution of (a) evaporation in the REF^{CLIM} simulation (left) and the difference between the SEN^{CLIM} and the REF^{CLIM} simulations (right), and (b) precipitation in the REF^{CLIM} simulation (left) and the difference between the SEN^{CLIM} and the REF^{CLIM} simulations (right). The period 2004 to 2013 is considered.

(a) (b)

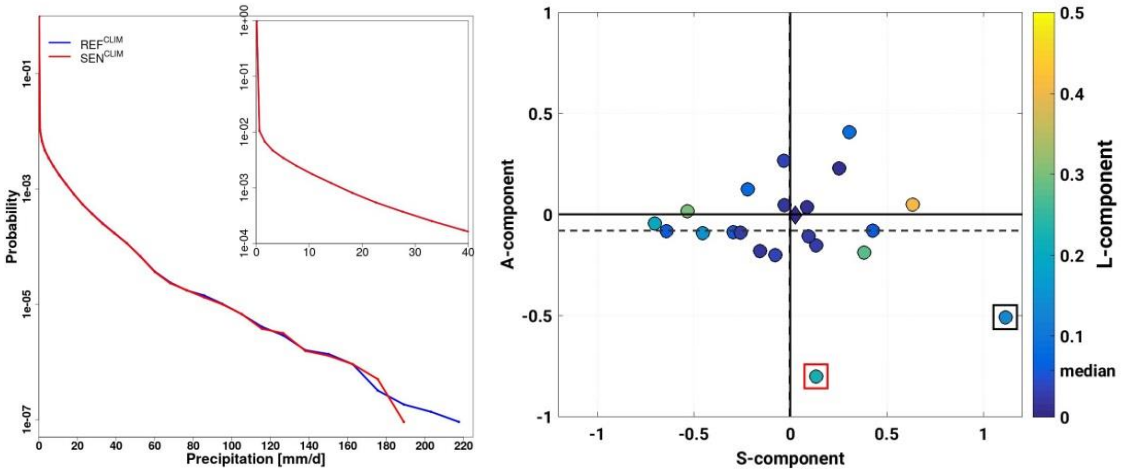

Figure 6: (a) Probability density function of daily precipitation intensities. All grid points in the investigation domain (Figure 1) and the period 2004 to 2013 are considered. (b) SAL diagram between REF^{CLIM} and SEN^{CLIM} simulations. Every circle corresponds to a simulated heavy precipitation event (listed in Table 1). The diamond (close to the zero-zero) illustrates the mean of all events. A-component (amplitude), S-component (structure), L-component (location). The inner colour indicates the L-component. Boxes point out the two events examined in this study, CASE1 and CASE2 (see section 3.2).

1039

1040 (a)

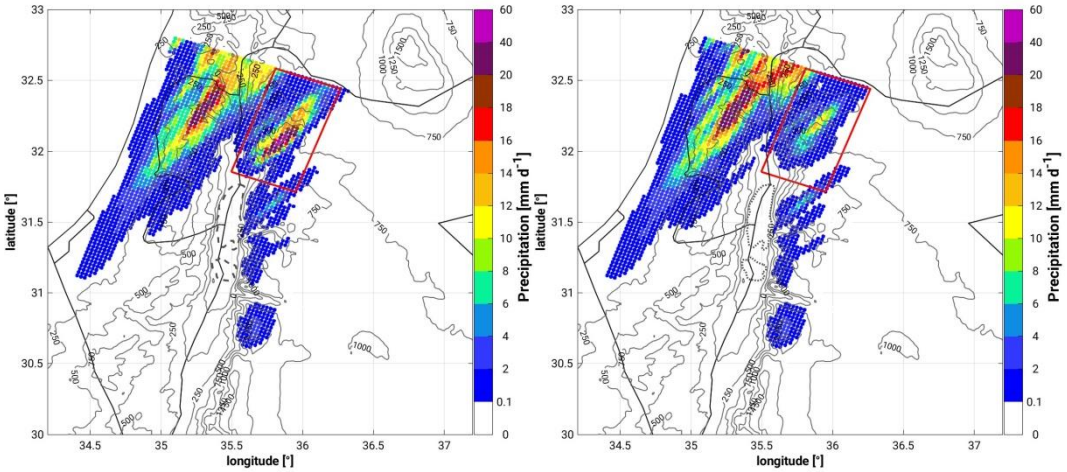

1041

1042 (b)

1043

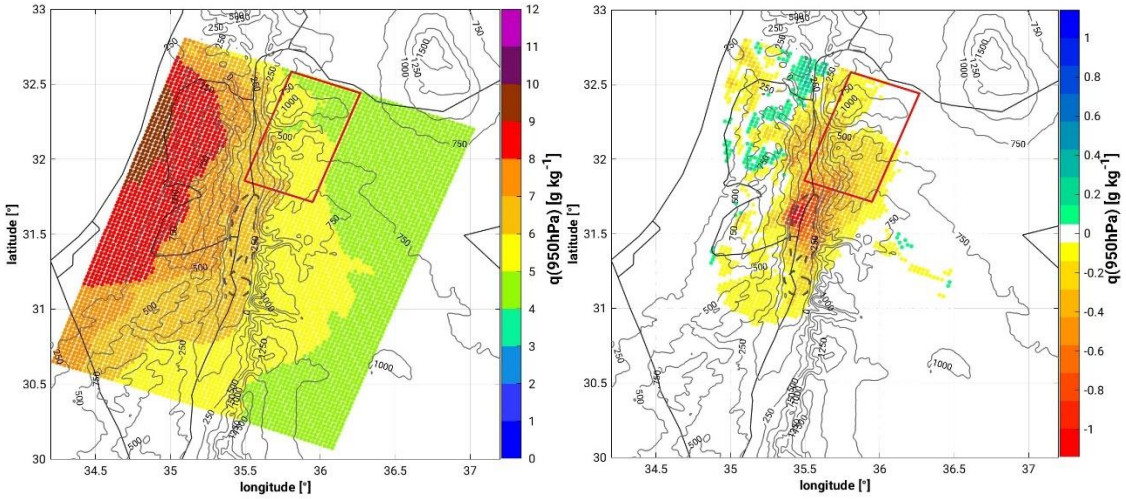

1044
1045

1046

1047

1048

1049

1050

1051

1052

(c)

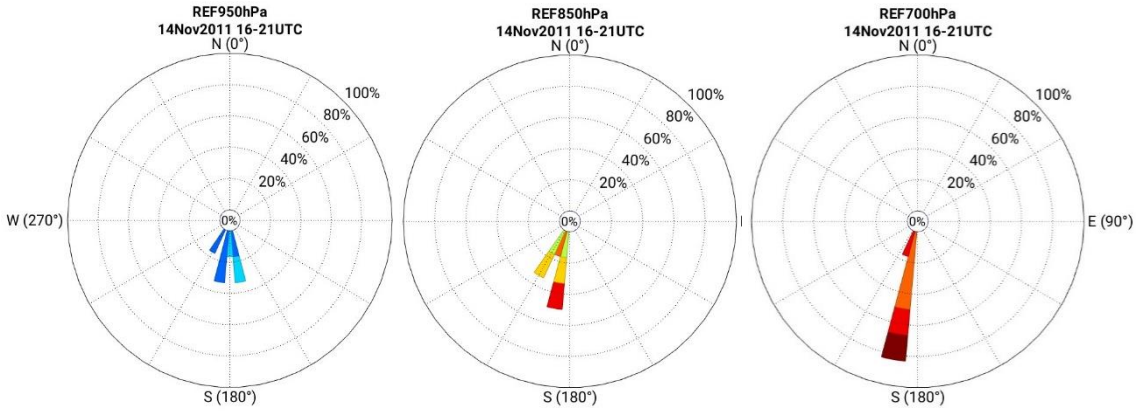
REF950hPa
14Nov2011 16-21UTC
REF850hPa
14Nov2011 16-21UTC
REF700hPa
14Nov2011 16-21UTC
N (0°)
E (90°)
S (180°)
W (270°)
20%
40%
60%
80%
100%
0%

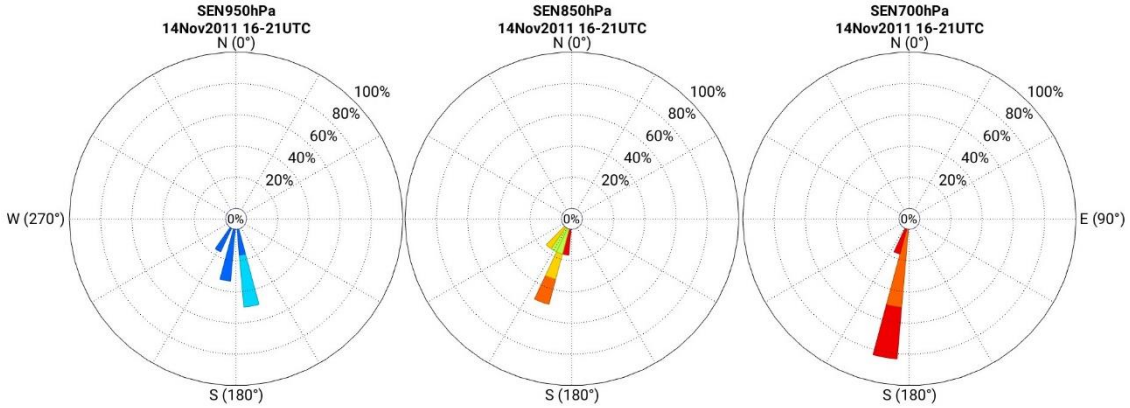
SEN950hPa
14Nov2011 16-21UTC
SEN850hPa
14Nov2011 16-21UTC
SEN700hPa
14Nov2011 16-21UTC
N (0°)
E (90°)
S (180°)
W (270°)
20%
40%
60%
80%
100%
0%


Wind Speeds in m/s
$W_S \geq 15$
$12.5 \leq W_S < 15$
$10 \leq W_S < 12.5$
$7.5 \leq W_S < 10$
$5 \leq W_S < 7.5$
$4 \leq W_S < 5$
$3 \leq W_S < 4$
$2 \leq W_S < 3$
$1 \leq W_S < 2$
$0 \leq W_S < 1$

Figure 7: Spatial distribution of (a) 24-h accumulated precipitation from 14.11 09 UTC to 15.11 08 UTC from the $REF^{14.11}$ simulation (left) and the $SEN^{14.11}$ simulation (right) and (b) specific humidity below 950 hPa, from the $REF^{14.11}$ simulation (left) and the difference between the $REF^{14.11}$ and $SEN^{14.11}$ simulations, as a mean for the 6-h period prior to convection initiation in the target area (14 November 16 UTC to 21 UTC), and (c) wind conditions at 700 hPa, 850 hPa, and 950 hPa (no relevant differences with respect to the 10-m field) for the same time period. Wind roses are centred at about 35.82°E-32.07°N in our target area.

(a)

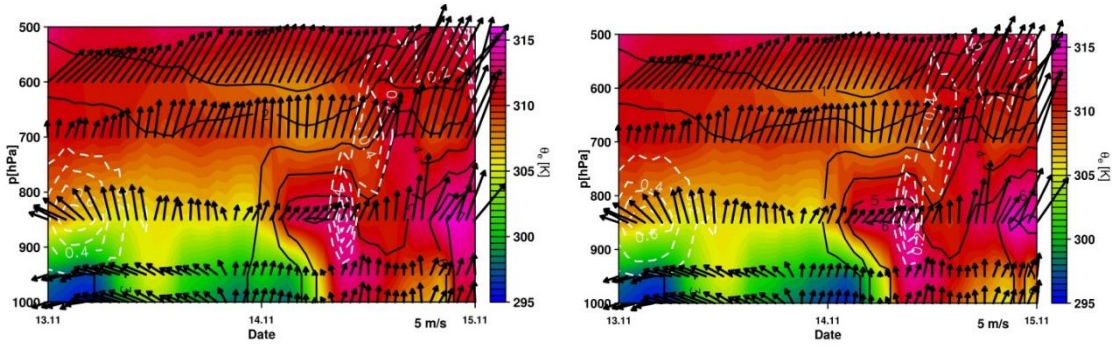

(b)

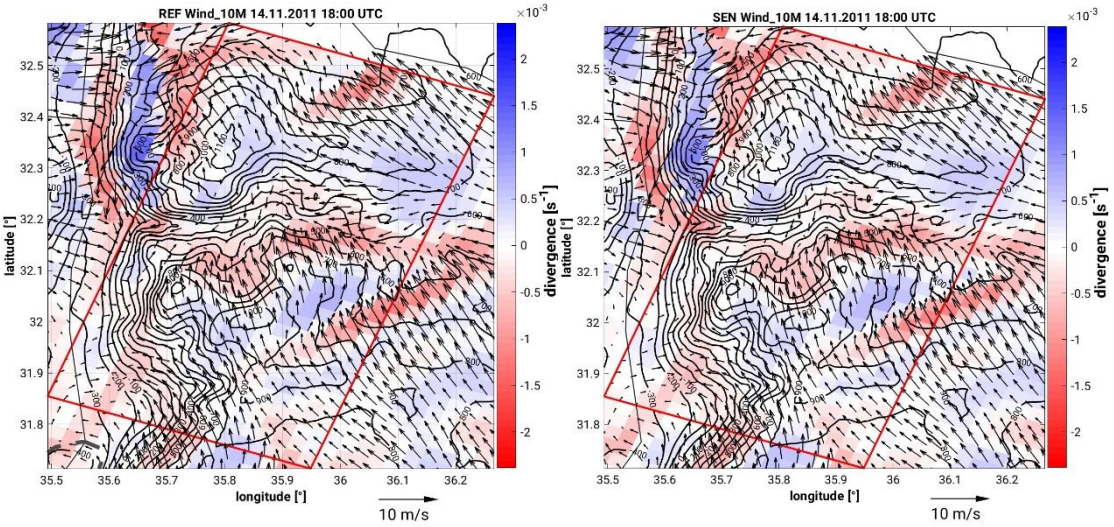

Figure 8: (a) Vertical-temporal cross-section of equivalent potential temperature (colour scale; K), specific humidity (black isolines; g/kg), horizontal wind vectors (north-pointing upwards, m/s) and vertical velocity (white dashed contours with 0.1 m/s increments) of the REF$^{14.11}$ (left) and SEN$^{14.11}$ (right) simulations, over a representative grid point in the sub-study region, 32.05°N 35.79°E. (b) Spatial distribution of 10-m horizontal wind (wind vectors; m/s) and corresponding divergence/convergence field (colour scale; s^{-1}) at 18 UTC on the 14 November 2011 from the REF$^{14.11}$ (left) and SEN$^{14.11}$ (right) simulations.

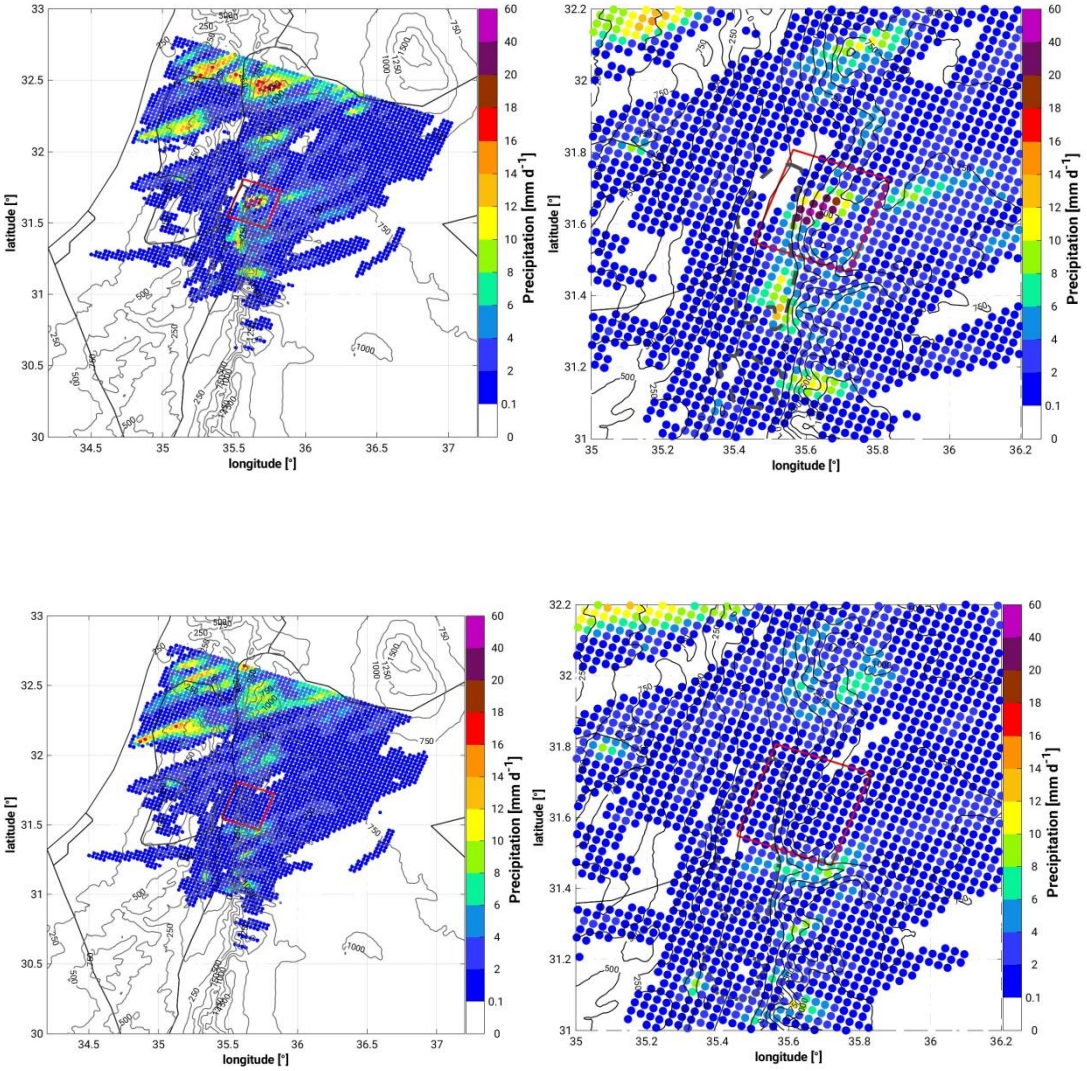

Figure 9: 24-h mean spatial distribution of precipitation from the REF$^{19.11}$ simulation (top-left; zoom top-right) and the SEN$^{14.11}$ simulation (bottom-left; zoom bottom-right) for the period 18 November 2011 11 UTC to 19 November 2011 10 UTC.

1127

1128 (a)

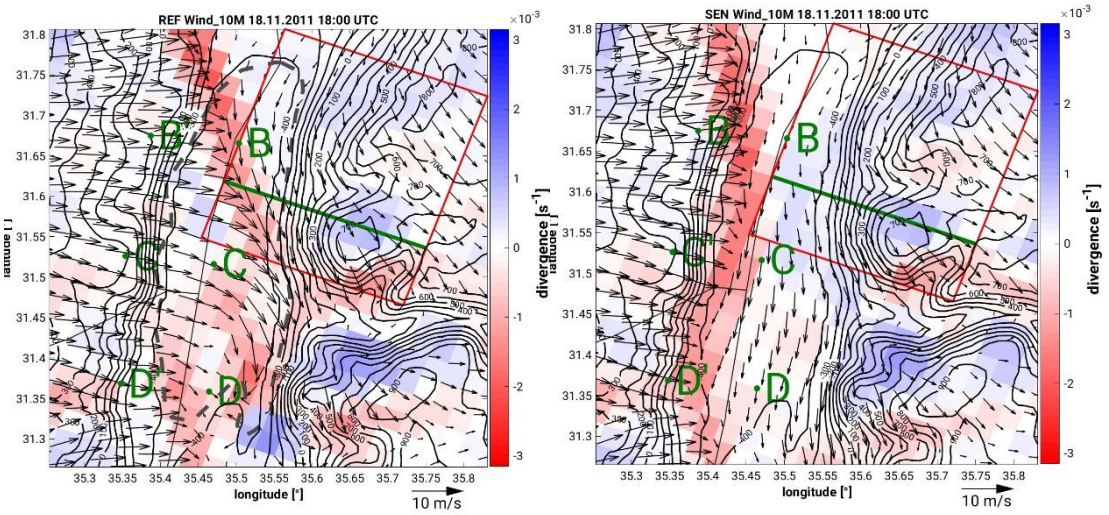

1129

1130 (b)

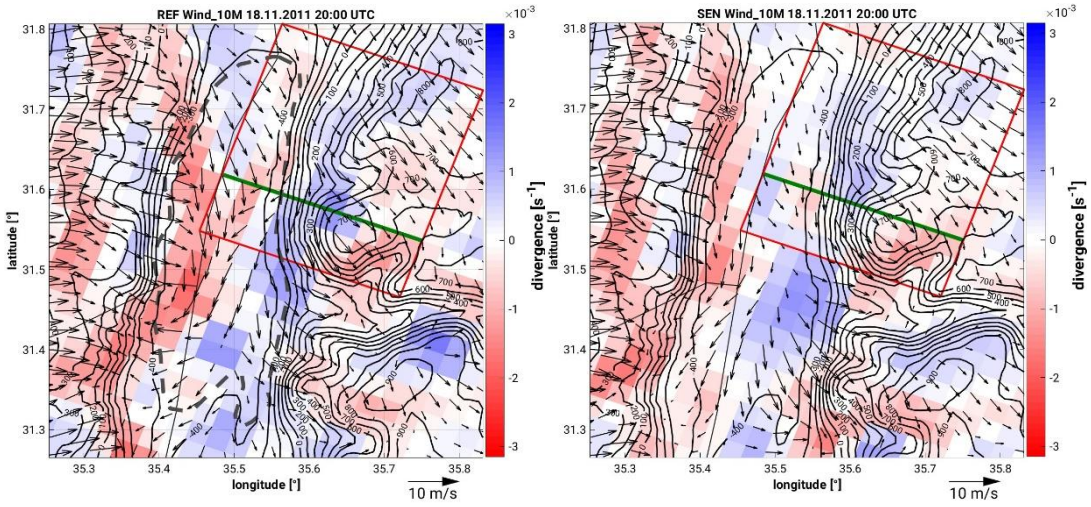

1131

1132

1133

1134

1135

1136

1137

1138

1139

(c)

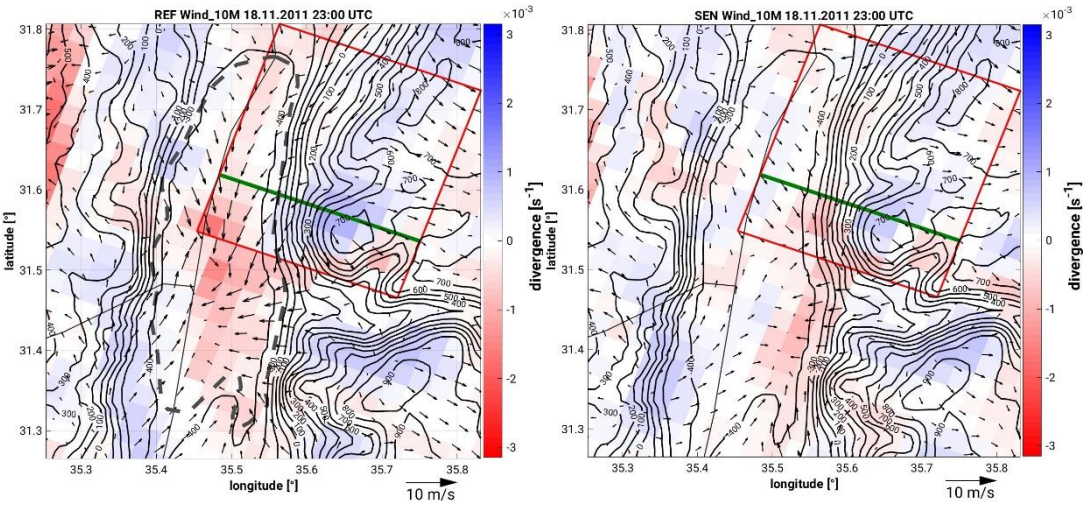

(d)

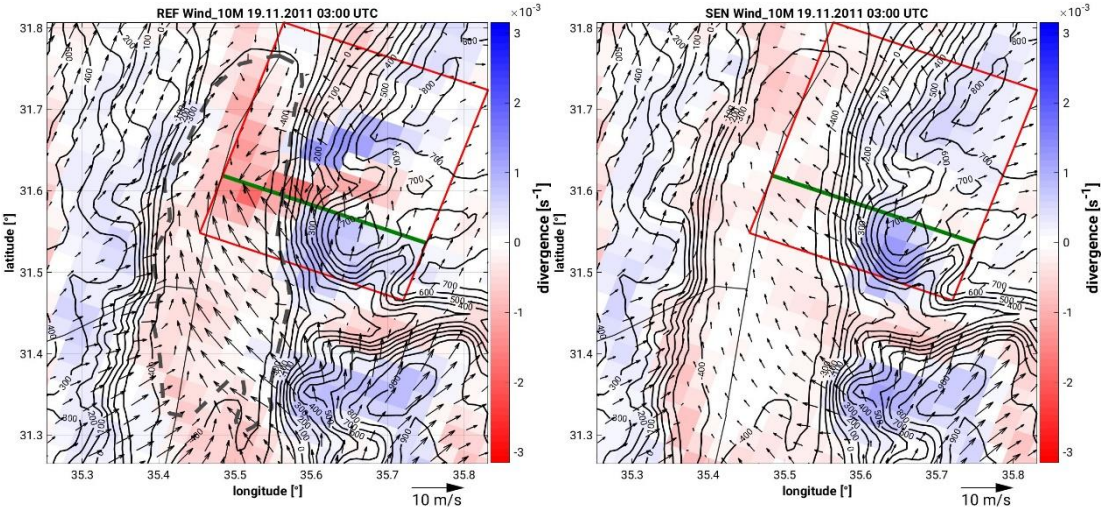

Figure 10: Spatial distribution of 10-m horizontal wind (wind vectors; m/s) and corresponding divergence/convergence field (colour scale; s^{-1}) at 18 UTC, 20 UTC, 23 UTC on the 19 November, and 03 UTC on the 20 November 2011 from the REF$^{14.11}$ (left) and SEN$^{14.11}$ (right) simulations. The topography is indicated by the black full isolines. The transects (B-C-D and B'-C'-D') corresponding to the locations in which temperature comparisons are made are indicated in Figure 10a. The green line indicates the position of the vertical cross-section in Figure 11.

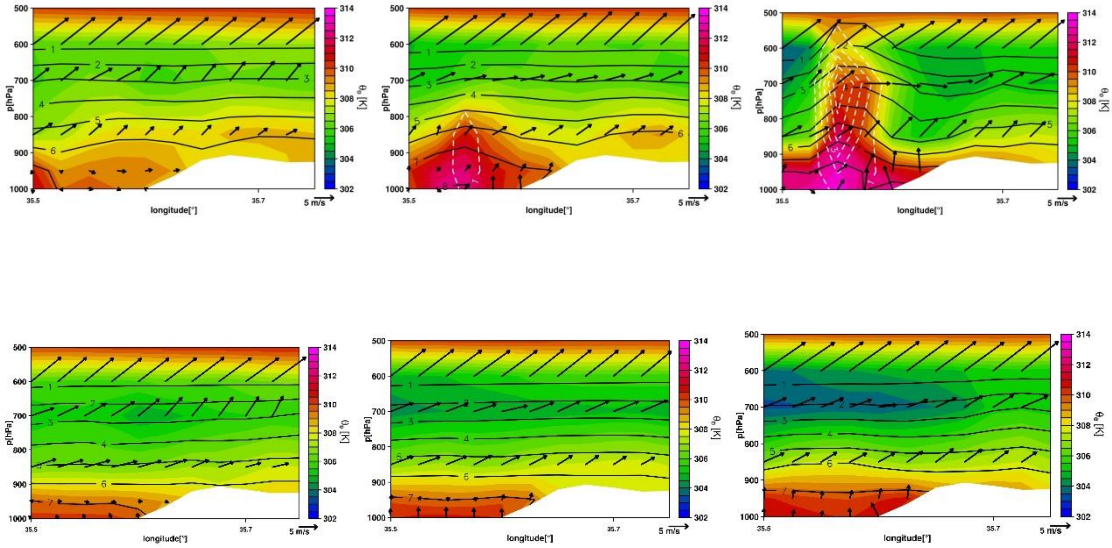

Figure 11: Vertical cross-section of equivalent potential temperature (colour scale; K), specific humidity (black isolines; g/kg), horizontal wind vectors (north-pointing upwards, m/s) and vertical velocity (white dashed contours with 1 m/s increments) of the REF[14.11] (top) and SEN[14.11] (bottom) simulations at 01 UTC (left), 02 UTC (middle) and 03 UTC (right). The location of the cross-section is indicated in Figure 10.